Duncan W. Haldane
Department of Mechanical Engineering,
University of California,
Berkeley, CA 94720
e-mail: dhaldane@berkeley.edu

Carlos S. Casarez
Department of Mechanical Engineering,
University of California,
Berkeley, CA 94720

Jaakko T. Karras
Robotic Actuation and Sensing Group,
NASA Jet Propulsion Laboratory,
Pasadena, CA 91101

Jessica Lee
Department of Mechanical Engineering,
University of California,
Berkeley, CA 94720

Chen Li
Department of Electrical Engineering and
Department of Integrative Biology,
University of California,
Berkeley, CA 94720

Andrew O. Pullin
Department of Mechanical Engineering,
University of California,
Berkeley, CA 94720

Ethan W. Schaler
Department of Electrical Engineering and
Computer Sciences,
University of California,
Berkeley, CA 94720

Dongwon Yun
Department of Electrical Engineering and
Computer Sciences,
University of California,
Berkeley, CA 94720

Hiroki Ota
Department of Electrical Engineering and
Computer Sciences,
University of California,
Berkeley, CA 94720

Ali Javey
Professor
Department of Electrical Engineering and
Computer Sciences,
University of California,
Berkeley, CA 94720

Ronald S. Fearing
Professor
Department of Electrical Engineering and
Computer Sciences,
University of California,
Berkeley, CA 94720
e-mail: ronf@eecs.berkeley.edu

Integrated Manufacture of Exoskeletons and Sensing Structures for Folded Millirobots

Inspired by the exoskeletons of insects, we have developed a number of manufacturing methods for the fabrication of structures for attachment, protection, and sensing. This manufacturing paradigm is based on infrared laser machining of lamina and the bonding of layered structures. The structures have been integrated with an inexpensive palm-sized legged robot, the VelociRoACH [Haldane et al., 2013, "Animal-Inspired Design and Aerodynamic Stabilization of a Hexapedal Millirobot," IEEE/RSJ International Conference on Robotics and Automation, Karlsruhe, Germany, May 6–10, pp. 3279–3286]. We also present a methodology to design and fabricate folded robotic mechanisms, and have released an open-source robot, the OpenRoACH, as an example implementation of these techniques. We present new composite materials which enable the fabrication of stronger, larger scale smart composite microstructures (SCM) robots. We demonstrate how thermoforming can be used to manufacture protective structures resistant to water and capable of withstanding terminal velocity falls. A simple way to manufacture traction enhancing claws is demonstrated. An electronics layer can be incorporated into the robot structure, enabling the integration of distributed sensing. We present fabrication methods for binary and analog force sensing arrays, as well as a carbon nanotube (CNT) based strain sensor which can be fabricated in place. The presented manufacturing methods take advantage of low-cost, high accuracy two-dimensional fabrication processes which will enable low-cost mass production of robots integrated with mechanical linkages, an exoskeleton, and body and limb sensing. [DOI: 10.1115/1.4029495]

1 Introduction

An insect's exoskeleton is an ideal model system for studying integrated structures in nature. It provides structural support,

Manuscript received August 16, 2014; final manuscript received December 23, 2014; published online February 27, 2015. Assoc. Editor: Aaron M. Dollar.

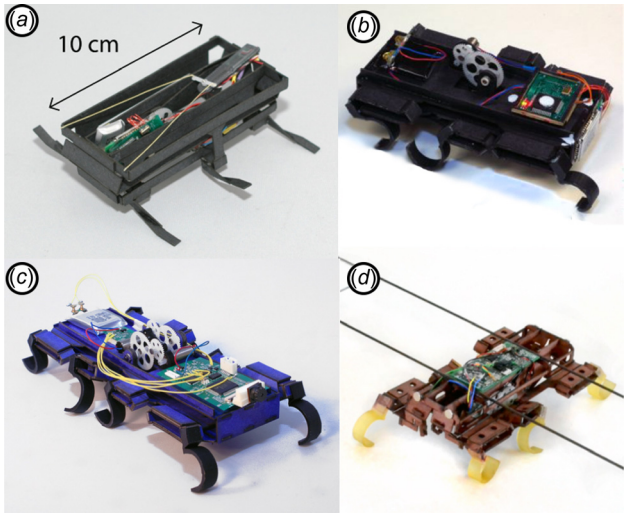

Fig. 1 Example SCM [7]. (*a*) DASH [9], (*b*) DynaRoACH [10], (*c*) OctoRoACH [8], and (*d*) VelociRoACH [11].

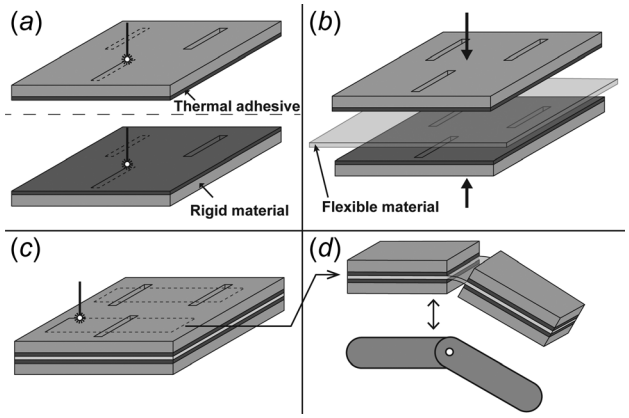

Fig. 2 Overview of the SCM process. (*a*) Holes for flexures are laser cut into a rigid material/thermal adhesive sandwich. (*b*) The layers of rigid material are aligned, and bonded to a flexible layer. (*c*) SCM parts are released with a final laser cutting step. (*d*) An SCM component, and its jointed rigid body approximation.

anchors actuators, is used for locomotion as well as sensing, and provides protection for the animal. Many insects and arthropods have integrated anisotropic spines which enable climbing and locomotion on sparse terrain [1]. More recent research has found that shape and compliance of the exoskeleton plays a part in higher level locomotory behavior. Discoid cockroaches use their flexible streamlined bodies to easily traverse cluttered terrain [2]. The integrated structures in the exoskeletons of insects enable sensory and perceptive behaviors. Robots with these same abilities will be more robust while operating in unknown environments.

In particular, we seek to enable these behaviors for palm-sized robots designed to operate in rough terrain, such as those shown in Fig. 1. Robots at this scale have several advantages over larger robots. It is easier for humans or other robots to deploy them. They can access small crevices that would be inaccessible to larger systems. Smaller systems can be inherently more robust than larger ones [3], and materials which would be too weak or compliant in a large robot are readily applicable at the smaller sizes. The limitation of these smaller robots, however, is that the integration of the type of sensing, protective, and locomotory structures that are seen in nature cannot be accomplished with traditional manufacturing methods. Novel and alternative manufacturing methods advance the field toward integrating these structures into small robots.

1.1 Background. The SCM process was developed as a way to fabricate mechanisms for microscale robots [4,5]. Traditional machine elements such as bushings or bearings do not scale down well in size, and greatly increase cost with higher precision. The SCM process replaces these components with flexural hinges that approximate revolute joints (see Fig. 2). SCM structures are produced using planar laser cutting processes. The process was introduced with cardboard by Hoover and Fearing [6] and composite materials in Wood et al. [7]. Its distinguishing feature is that the rigid links and flexible joints are cofabricated with layered laminar processes.

Although originally developed for microscale robots, recent work has expanded SCM up to palm-size robots. These legged robots weigh between 15 and 30 g, and are capable of crawling [8], running [9–11], turning [12,13], and climbing [14,15]. Integrated kinematic linkages made with the SCM process drive the appendages of these robotic platforms. These linkages produce the desired kinematic output for all of the appendages using only a few actuators which reduces the complexity of the system.

SCM has advantages which relate to the manufacturability of robots made with the process. Because SCM is a layered approach, it is compatible with reel-to-reel manufacturing, giving the designer good confidence that the SCM portion of the robot under development is compatible with extant mass-manufacturing techniques. When designing products for assembly, it is important to reduce the number and diversity of parts and to make the parts easy to assemble [16]. Unlike traditional manufacturing methods, SCM parts which require relative kinematic motion can be readily combined, thereby decreasing the overall part count. The entire kinematic structure of the robot is fabricated from only a few materials. Therefore, the diversity of required components for making a wide variety of robots is minimized, which is desirable for high-mix manufacturing environments.

The layered nature of the SCM process allows specialized materials to be incorporated during the manufacture of robotic mechanisms. This inherent extensibility allows for the manufacture of more complex integrated structures than have previously been explored. The next step for palm-sized robots is to use SCM to integrate protective and sensing structures that will allow extended field operation.

1.2 Paper Overview. This work focuses on manufacturing methods for SCM mechanisms with integrated structures for sensing, protection, and attachment. In terms of paper organization, each subsystem has been compartmentalized into its own section. To facilitate the design of new robots made with SCM, we present design guidelines in Sec. 2. A method to rapidly produce palm-sized SCM robots is given in Sec. 3. Suitable materials for SCM are discussed in Sec. 4. Thermoformed shells for aiding obstacle traversal and protecting SCM robots are presented in Sec. 5. Anisotropic claws for improving climbing performance are demonstrated in Sec. 6. Sensing structures are also integrated into the design of SCM robots. Ground obstacles and contact forces from obstacles met head-on can be detected using binary hair sensor arrays and analog tactile bumpers detailed in Sec. 7. Also, contact forces of individual legs can be measured using flexible piezoresistive strain gauges integrated into lightweight fiberglass legs, as described in Sec. 8.

2 How to Design SCM

The SCM process accelerates the design of robotic mechanisms but it requires some specialty design knowledge.[1] Numerous previous works have discussed the kinematic design of SCM

[1]Software is currently being developed to automate some of the design process (e.g. http://www.popupcad.org). We contend that even when the software is in a fully functional state, users will benefit from knowledge of good design practices.

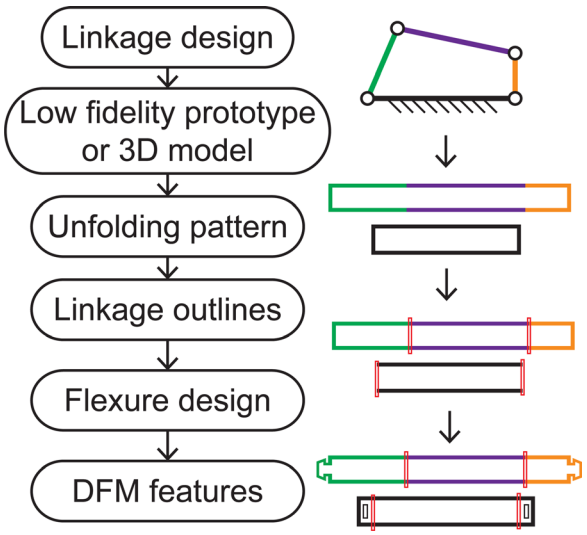

Fig. 3 A summary of the SCM design process, and CAD workflow. The cartoon on the right shows how CAD would be generated for a simple SCM four-bar linkage. The links are color coded for clarity, and the red rectangles represent the flexures as they would be cut in Fig. 2(*a*).

structures, but few details have been given on how to effectively utilize computer aided design (CAD) tools during the SCM design process. Frequently only the final design is presented (e.g., Fig. 4(*b*)) without supporting details of the design process (e.g., Fig. 3), or design files for the robotic mechanism (Fig. 4(*a*)). In order to facilitate the reproduction of our design and manufacturing process, we give those details here.

With this publication, we have open-sourced designs for a hexapedal robot, the "OpenRoACH"[2] which is shown in Fig. 4(*b*). It is 15 cm long and has two degrees of freedom powered by an inexpensive, commercially available gearbox (Tamiya 70097). Other than the gearbox, all of the parts for the robot can be made on a laser cutter. We hope it will serve as a practical example of the practices described in this section.

Figure 3 shows an overview of the SCM design process. First the desired linkage is synthesized. This design problem has been well addressed in the previous works (e.g., Refs. [9,10,17], and [18]). After the linkage is synthesized, its 3D geometry is determined, and a convenient unfolding pattern which maps that spatial linkage to 2D geometry is specified. Low fidelity prototypes and 3D kinematic models are useful tools to facilitate this step. After the unfolding pattern is generated, the CAD which will be used to manufacture the SCM mechanism is produced. The cartoons in Fig. 3 show this process. The outlines of the links are drawn, then rectangular cutouts for the flexures are added. The design of these flexural pivots is important because they have nonideal behavior as compared to ideal pin-joints. They cannot make full revolutions. They do not support large compressive loads, and they have non-negligible off axis torsional compliance. These nonideal properties must be considered when designing SCM flexures. This subject has been treated in detail by previous publications [7,19], which serve as a useful resource for the SCM designer. The last step in the design process is to add features which make the mechanisms easy to assemble. These features, such as tab-hole connections, or sites for glue deposition are discussed in Sec. 3. The production of this CAD is assisted by macros which automate portions of the drawing process.

We use Autodesk's AUTOCAD software to design our robots. There are several features of the program which aid the creation of SCM structures. First, geometry for each separate cutting operation can be kept on distinct layers, and color coded for clarity.

[2]https://github.com/dhaldane/OpenRoACH

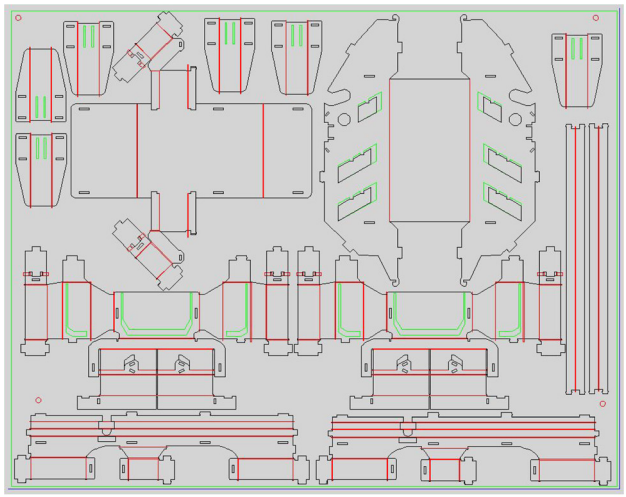

(*a*)

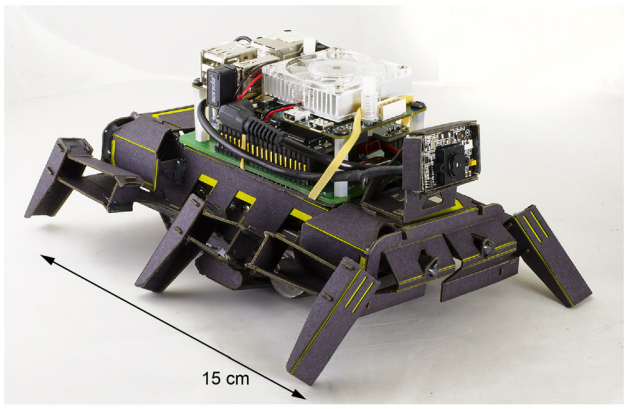

(*b*)

Fig. 4 The open source SCM robot, OpenRoACH. (*a*) CAD layout of OpenRoACH SCM parts. (*b*) The OpenRoACH carrying a computational payload.

Second, each component of the robot can be made into a "block," Each part in Fig. 4(*a*) is a block, repeated instances of the parts are merely copies of that same block. A block in AutoCAD is a group of geometry which has a name, and is editable separately from the rest of the drawing. Each instantiation of the same block in a drawing is updated when a change is made in the block editor. This means that a designer can have components placed in a reference configuration, as well as a fully populated layout for the laser cutter as shown in Fig. 4(*a*). Given the complexity of the planar geometry of SCM parts, we prefer to work without parametric constraints. Again, please view the OpenRoACH drawings for a better understanding of these details.

3 Designing SCM Parts for Manufacturability

Recent work presents methods to facilitate the assembly of microscale SCM robots [20,21]. Whereas previous robots took days to assemble under a microscope, this new process (branded as pop-up book MEMS or printed circuit MEMS) can assemble robots of diverse morphology (e.g., Refs. [21] and [22]) in just a few steps. Pop-up MEMS uses secondary mechanisms which are cofabricated with the robot to fold up the structure and hold it while it is bonded. This greatly accelerates the assembly process but has several drawbacks. Time must be invested to design the assembling mechanism. This time cost is quickly recouped if multiple microscale robots are assembled, but it does increase the design overhead for each prototype of the robotic platform (to a

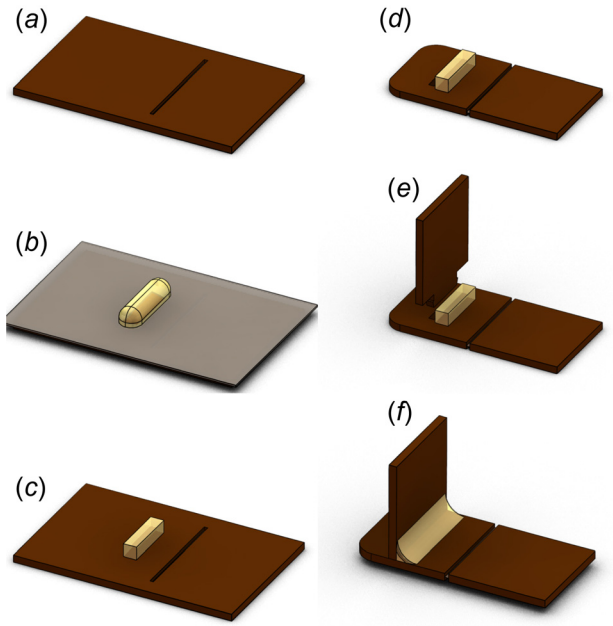

Fig. 5 The self-fixturing / reflow process. (*a*) Cardboard sandwich with cutouts for flexure joints. (*b*) Thermal adhesive is applied over a Teflon template. (*c*) The template is removed leaving thermal adhesive on the cardboard. (*d*) Part outlines and tab holes are laser cut into the cardboard. (*e*) Parts are assembled. (*f*) Entire assembled robot is placed in oven to reflow thermal adhesive.

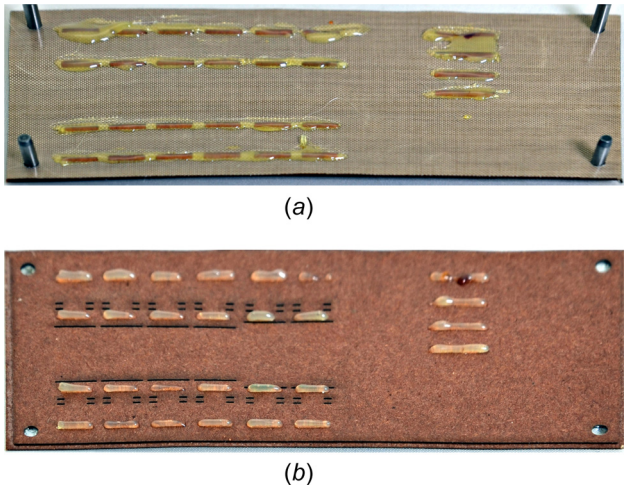

Fig. 6 Images showing hot melt adhesive applied with a Teflon template. (*a*) The Teflon template with thermal adhesive applied (as in Fig. 5(*b*)). (*b*) Carboard base after template is removed (as in Fig. 5(*c*)).

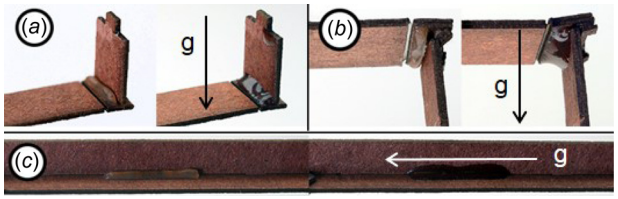

Fig. 7 Images of joints before and after reflow. Arrows show orientation of gravity as parts were reflowed (*a*) adhesive facing up; (*b*) adhesive facing down; and (*c*) adhesive strip aligned with gravity. These images demonstrate that the reflow process is not sensitive to the orientation of the parts.

sufficient degree such that design of the pop-up mechanism is sometimes left for future work [18]). The second drawback is that the mass of the support structure relative to the platform does not favorably scale up with robot size. We calculate that 94% of the material used to manufacture a 90 mg flying platform [21] was used for the support structure or removed as waste. An isometric scaling of this process implies that there would be over 200 g of waste material every time a 12 g SCM transmission for a running robot [11] was produced. Fortunately, these larger robots can be readily assembled by hand. We present a new assembly method wherein a robot's pieces are snapped together by hand, and hold themselves in place while being bonded with thermal adhesive in a batch process.

3.1 Methods and Materials. The thermal adhesive batch reflow process is shown in Figs. 5 and 6. First the material for the flexures is removed, and the rigid and flexible layers are sandwiched together as shown in Fig. 2. A Teflon template is then aligned over the sandwich, and a layer of thermal adhesive is applied by hand with a hot glue dispenser. The template controls where and how much glue is applied, so the glue dispensing need not be accurate nor highly controlled. This adhesive (Packaging hot glue, McMaster) is specially formulated for bonding fibrous natural materials. The Teflon template is then removed while the adhesive is warm, leaving glue deposited in only specific locations. The part outlines and holes for interlocking tabs are then laser cut, and the parts are assembled. After assembly the entire SCM structure is placed in an oven at 135 °C for 3 min. This reflows the hot-melt adhesive, reinforcing the tabbed joints, as shown in Fig. 7. The orientation of the parts during reflow is unimportant,[3] which simplifies the design process.

This assembly method relies on the robot's parts to self-fixture, i.e., hold their shape while being glued, without any external jigging. For this purpose, we use tabs like the one in Fig. 5(*e*) for all 90 deg connections. The insertion stiffness of these tabs is sufficient to maintain the robot's configuration while it connections are bonded during reflow. This critical feature allows multiple robots to be reflowed at once, in the aforementioned batch process. OpenRoACH uses these tabs to facilitate its assembly.

4 Making Larger and Stronger Folded Robots

For small SCM robots (10–45 g), we have found that cardboard (Pacon 4-ply Railroad Board) is functional as a rigid material. At this scale, the strength of cardboard is not a limiting factor, and it is lightweight, stiff, and readily available. As a flexible material, we use 25 μm polyethylene terephthalate (PET) film. These layers are bonded with hot-mount adhesive (Octavia) in a heated roll laminator (Pro-Lam PL-1200HP). Numerous robots [8–11,13–15] use these simple materials.

Although functional for robots of small size, cardboard and PET are best used for prototyping, not for robots intended for extended field operation. Over time the PET flexures will tear, and the cardboard beams will delaminate. In addition, these materials are not strong enough to use for larger robots. In this section, we explore materials which allow larger and more robust SCM structures.

The first SCM process used a single material to make the entire mechanism [4]. In this process, stainless steel shim was cut with an UV ablation laser, then folded and glued into rigid beams which were connected by short flexural pivots in a process that took up to two days. Advances were made in the development of jigs for automated folding, and the manipulation of structures for

[3]This is not necessarily the case when using higher temperatures. The reflow temperature should be chosen such that the molten adhesive has the appropriate viscosity.

small robots [23]. The problem with this version of SCM was that one material had to act as both a rigid element and a flexible element, which limits the pool of appropriate materials. An insect's exoskeleton is also composed of (largely) one material: chitin. However chitin in rigid portions of an exoskeleton is selectively reinforced with calcium carbonate [24] which forms a rigid composite. The exoskeleton therefore has effectively two materials: one rigid used for support, and one flexible used for joints.

In 2003, Wood et al. [5] extended the SCM process to use multiple materials, one rigid (carbon fiber reinforced polymer) and one flexible (polyimide). This specialization of materials decreased the assembly complexity and increased the performance of SCM robotic structures. At the time of writing, dynamic SCM microrobots [18,22,25] still use these same basic materials. Recent work in folded robots has revisited one material structures [26,27], citing alignment as a difficult problem. We have found that dowel pins enable an alignment accuracy of 8 μm between layers, which is sufficient for our robots which use a nominal flexure length of 300 μm.

SCM robots above the microscale, such as the 2.4 g crawler mini-RoACH [28], or a 1.1 g jumping robot [29] use fiberglass as a rigid material. Larger SCM structures were made out of fiberglass because it can be quickly cut with an infrared laser. Carbon fiber is best cut with a UV ablation laser, and UV ablation lasers on the market today have more limited working areas than their infrared counterparts, take longer to cut, and are more expensive.

4.1 Figures of Merit for SCM Materials. One limit which we impose on our choice of material is that it be readily machinable in an infrared laser cutter. This restriction ensures that our fabrication methods require minimal specialty equipment. With this limitation in mind, we explore options for both the rigid layers and the flexible layer.

We seek to establish figures of merit which relate material properties to high-quality folded robotic mechanisms. For kinematic reliability, it is important that the rigid material be lightweight and rigid. We therefore seek maximum bending stiffness for minimum weight for the rigid material. This is equivalent to maximizing the figure of merit $Q_b = E^{1/2}/\rho$, where E is the flexural modulus of the material, and ρ is the density. We also consider the failure strength figure of merit $Q_f = \sigma_f^{2/3}/\rho$ where σ_f is the failure strength. Maximizing this figure of merit increases the force capacity of the resultant mechanism. There are other practical concerns for the rigid material such as its delamination strength, how easy it is to bond, the complexity of its production, and the toxicity of the products from its combustion (very relevant when the material is cut with an infrared laser).

From the flexible material, we desire maximum fracture toughness (or tear strength for a fabric), minimum damping, and minimum energy storage. Some energy storage in the joints may be desirable at times, but it exacerbates nonlinear force generation in the transmission and we find that it is usually best minimized. Another practical consideration is how easy the flexible material is to bond. For example, polypropylene would make excellent flexures (and is commonly used in injection molding for such a purpose) but it is difficult to bond without thermal welding processes.

4.2 Methods and Materials. We evaluated several new rigid material options for the SCM process. Sandwich composites have large stiffness-to-weight ratios so we explored sandwich materials that met our fabrication criteria. Balsa wood is a good core material because it is stiff, low density, and cuts well with an infrared laser. Face-sheets, which are more difficult to cut than the core material, cause fabrication difficulties. For example, G10 fiberglass panels are cuttable with an infrared laser, but the high power required to cut a G10-balsa sandwich composite burns out the core material. We therefore fabricated several sandwich composites with easy to cut face-sheets.

We used 1/16th balsa (Midwest Products) for the core material. Composites with three different face-sheets were made. The first

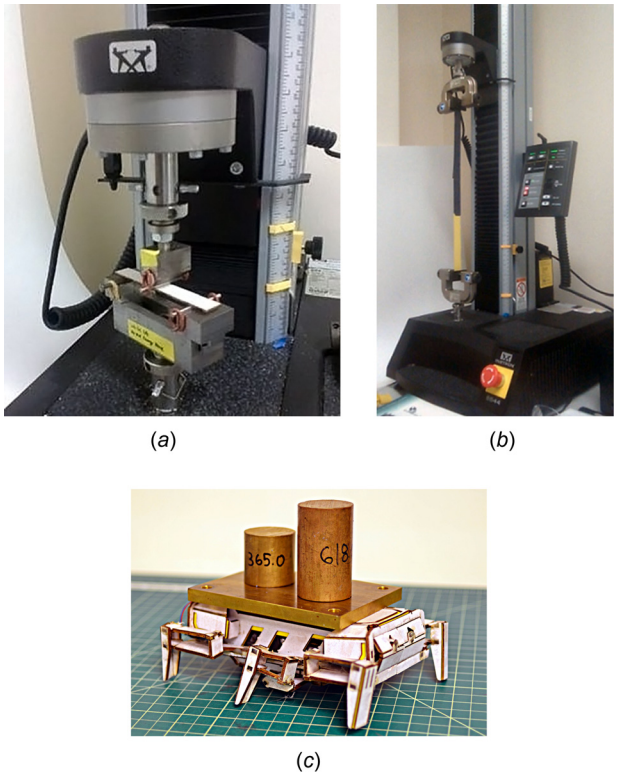

(*a*) (*b*) (*c*)

Fig. 8 Images of experimental setups for material tests. (*a*) Bending test; (*b*) delamination test; and (*c*) crush test for the B-P-CA OpenRoACH, shown with a 1.9 kg load.

(B-PET) was made using 25 μm PET film adhered to the balsa core with hot mount thermal adhesive (Octavia) laminated at 210 °F. The second face-sheet (B-P) was 20 lb copy paper. To make this composite we spread white glue on each side of the balsa in as thin a layer as possible, and then applied the copy paper with a Nylon squeegee. The composite was then left to dry with small weights on top to avoid warping. The third face-sheet (B-P-CA) was prepared identically to the second but after drying, a thin layer of cyano-acrylate adhesive (Loctite 495) was applied to the surface of the copy paper with a Nylon squeegee.

Three-point bending tests (ASTM D3043, shown in Figs. 8(*a*) and 9) performed in an Instron 5544 material testing machine established the flexural modulus and failure stress of each material.[4] The balsa wood specimens were aligned such that the grain of the wood took the bending load.

For the flexible material, we evaluated the delamination strength of its bond to the rigid material candidates with a peel test (ASTM D903, shown in Fig. 8(*b*)). Samples of uncoated 1.1 oz ripstop Nylon[5] (Ripstop by the Roll), and PET film (McMaster) were laminated to both cardboard and balsa wood with hot-mount thermal adhesive (Octavia) in a hot-roll laminator at 300 °F.

Ripstop nylon is difficult to bond with traditional methods. The strength of the bond is increased by laminating the ripstop Nylon with hot-mount adhesive before including it in the composite sandwich. If a stronger bond is required, the Nylon should be dessicated prior to use. As a hydrophilic polymer, Nylon contains significant amounts of water which can interfere with the thermoplastic hot-mount adhesive. We thoroughly dessicated our ripstop Nylon in a vacuum oven at 25 inHg and 65 °C for 1 hr.

[4]Except cardboard, which did not fail in the bending test, because the specimen was too compliant for the bending gauge length. Tensile strength is given instead.

[5]Ripstop Nylon is used in the commercialized version of DASH [3] (made by DASH Robotics).

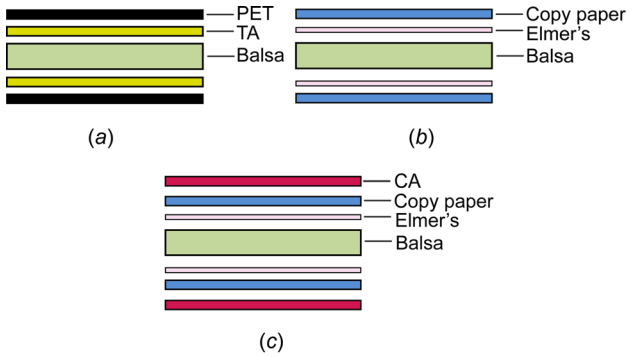

Fig. 9 Structure of composites: (*a*) balsa-PET (B-PET) composite; (*b*) balsa-paper (B-P) composite; and (*c*) balsa-paper-CA (B-P-CA) composite

Other processing conditions with nonvacuum ovens should also be adequate.

Another strong flexure material is Cuben fabric (Ripstop by the Roll). It consists of ultrahigh molecular weight polyethylene filaments (known commercially as Spectra, or Dyneema) embedded in a polyester matrix. It is not as strong as ripstop Nylon, but is easier to work with; it can be swapped with PET film in any extant design without modifying the build procedure.

4.3 Results. Properties for candidate rigid materials are shown in Table 1. From left to right the columns list the density, flexural modulus, yield strength, and the figures of merit for stiffness and strength. Note that these are effective bulk material properties for the entire laminate structure. All of the tested materials appear in this table, as well as several other candidate materials for which typical properties are given. As a comparison, properties for three common engineering materials (4140 Steel, Ti-6Al-4V Titanium, 0.6 fiber fraction UHM uniaxial carbon fiber), which are not easily cuttable with an infrared laser, are also given.

Because of its low density, balsa wood was the best performing material in terms of the stiffness figure of merit, Q_b. However, this only considers loading along the fiber axis; the compliance across the fibers is significantly greater. These orthotropic properties are not desirable for the SCM process. The composites made with balsa wood as a core were stiffer and more dense than the balsa alone. They are comparable in terms of the figures of merit. In absolute terms, however, the balsa-paper-CA (B-P-CA) composite was the stiffest and strongest of the three. These properties were a result of the isotropic face sheet, which mitigates the orthotropic properties of the balsa wood core.

Table 1 Rigid material properties

Material	ρ	E_B	σ_F		
Units	kg/m^3	GPa	MPa	Q_b	Q_f
Cardboard	806	0.93 ± 0.016	11.8 ± 0.3	0.01	0.0066
Balsa	84.1	0.85 ± 0.12	8.32 ± 1.7	0.35	0.048
B-PET	185	2.41 ± 0.29	22.1 ± 4.9	0.27	0.042
B-P	185	2.18 ± 0.19	17.8 ± 1.0	0.25	0.036
B-P-CA	229	2.81 ± 0.78	23.0 ± 3.5	0.23	0.035
[a]PET	1380	2.76	80.5	0.038	0.013
[a]GFRP[b]	1800	50	1400	0.12	0.070
[a]Steel	7850	200	415	0.057	0.007
[a]Titanium	4430	114	880	0.076	0.021
[a]CFRP[c]	1660	294	840	0.326	0.053

[a]Typical value.
[b]Glass fiber reinforced polymer.
[c]Carbon fiber reinforced polymer.

Table 2 Delamination strength

Material	Peel strength N/mm
Cardboard-nylon	0.132 ± 0.003
Cardboard-PET	0.095 ± 0.006
Balsa-nylon	0.097 ± 0.004
Balsa-PET	0.030 ± 0.003

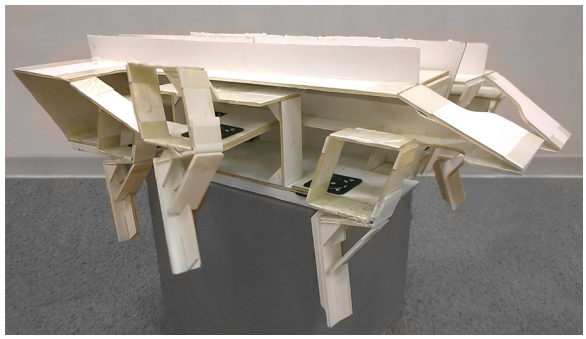

Fig. 10 A meter long hexapedal SCM robot made in the BIRDS lab at the University of Michigan. Developed by Devin Miller, Ian Fitzner, and Shai Revzen, with thanks to Stacie Desousa.

Of the materials which can be cut by an infrared laser, fiberglass has the highest strength figure of merit. However commercially available fiberglass board is typically reinforced with epoxy which produces harmful fumes when cut with an infrared laser. It should be noted that all tested materials outperformed cardboard in both categories.

The peel strength of the flexible material bonds is given in Table 2. All cardboard specimens failed by internal delamination which indicates a material limit has been reached for the bonding of these materials. Slightly more cardboard came off on the Nylon than the PET, which may explain the difference in peel strengths. The bonds to the balsa wood failed at the surface. The bond between Nylon and balsa was stronger than that between balsa and PET. The paper composites (B-P and B-P-CA) were also tested for delamination strength. However, the bond between the balsa wood and the paper was sufficiently strong such that the paper failed before delamination, so the delamination strength could not be assessed.

Based on our findings on new materials for stronger and larger legged robots, we built two OpenRoACH robots (See Sec. 2), one with cardboard and one with the B-P-CA composite. To evaluate the relative benefits of the two materials, we performed a static crush tests (shown in Fig. 8(*c*)) wherein weights were added to the robots until the chassis touched the ground. This test gives a measure of the robot's ability to carry loads. The cardboard robot withstood 780 ± 60 g before failure, the OpenRoACH made with the new B-P-CA composite withstood 3350 ± 250 g before failure. Series compliance in the mechanisms, causing deflection of the legs was the predominant failure mode in these tests.

Other materials can be used to further extend SCM to larger structures. Researchers at the University of Michigan[6] have worked to extend SCM up to the human scale as shown in Fig. 10. A sandwich composite material (Elmer's white poster board) allowed for a high-stiffness to weight ratio. The flexures were formed with fiber reinforced tape (3M 8959 and 3M 720). At this scale, the researchers found that special considerations had to be made for component stiffness, and some flexures required reinforcing structures to avoid buckling. These researchers have

[6]http://www.birds.eecs.umich.edu/teaching/senior-project-2013-scm/

shown that with appropriate material choice and design considerations, SCM can be extended to much larger structures than have been made previously.

5 Exoskeletons for Expendable Robots

In this section, we demonstrate the manufacturing of an integrated protective exoskeletal shell that is compatible with the SCM rapid prototyping process. The developed exoskeleton manufacturing process uses the adaptable thermoforming process to create a variety of shell shapes through CAD-driven laser cutting and 3D printing of molds. These mold prototyping processes allow for rapid, low-cost iteration of shell molds to accelerate from the proof-of-concept stages up through to field deployment. Thermoforming is cheap, quick, and the process produces shells that can be recycled. Our exoskeleton manufacturing process leverages thermoforming of multiple materials to produce a compliant structure that protects against falls, collisions, and other sources of potential damage from the environment. This structural shell is integrated with a flexible bag layer that seals the robot against water, sand, and mud during locomotion. The exoskeleton is integrated into the VelociRoACH while permitting mobility of the SCM linkages which drive the legs.

The main contribution of this section is the development of a thermoforming manufacturing process that adds environmental protection and field robustness to a broad array of underactuated robots, with careful consideration of weight reduction, minimal restriction of locomotion performance, and ease of assembly. The developed process uses rapid prototyping of molds for the benefits of supporting iterative design and reducing mold manufacturing costs. In addition, the process is scalable both in size and number of robots, subject to the size of the thermoforming tooling.

5.1 Background. Structures that protect robots against the environment and impacts have been designed and implemented for many years. In swimming robots where protection against water is a requirement, this has been implemented for at least two decades [30–33]. In miniature jumping [34] and flying [35,36] robots, and in many commercial quadrocopter drones [37,38], springy protective cages or hulls have also been implemented to absorb impact energy from collisions that occur after jumps, flight malfunctions, or during navigation of cluttered environments. Additionally, engineers have developed an anti-impact design for a wheeled robot that considers incorporating shock reduction into the structure, transmission, and suspension [39].

In the context of protective structures for vehicles and robots, thermoforming is a common manufacturing process. However, the application of thermoformed protective structures to centimeter-scale SCM robots is especially challenging because added weight to the robot has the cost of significantly reducing locomotion performance. For this reason, the thermoformed exoskeleton needs to be thin, compliant, and use minimal fasteners and adhesives.

In addition, the geometry of the SCM kinematic linkages makes it difficult to seal the robot against the environment without restricting the legs. Traditional methods for sealing against fluids, such as compressing a rubber gasket between two rigid components, are not feasible in this application because of the high weight costs.

With the above considerations in mind, this work aims to expand the application of water resistant and impact-reducing structures to lightweight robots.

5.2 Thermoforming for Integrated Robotic Structures. Thermoforming provides a means to fabricate a wide variety of integrated protective structures for robots. The vacuum-forming process is simple: a sheet of thermoplastic polymer is heated and then drawn over a mold with vacuum pressure, as shown in Fig. 11. The mechanical properties (e.g., stiffness and damping)

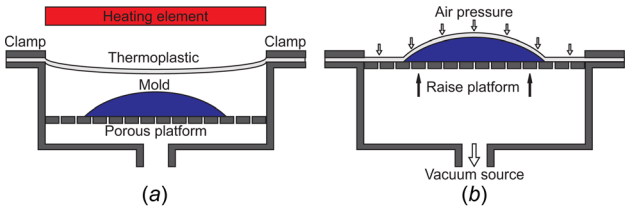

Fig. 11 Schematic of the thermoforming process. (*a*) Heating of a thermoplastic sheet softens it above a positive mold. (*b*) Pressure difference from a vacuum source forms the softened thermoplastic onto a positive mold into the desired shape.

of the protective structures can be tuned by adjusting the type and thickness of thermoplastic used. Vacuum-formed components are inexpensive and rapid to produce, similar to the SCM robots that they protect.

Three components are required to manufacture vacuum-formed parts: a thermoforming machine, a mold, and a thermoplastic sheet. We use the Formech Compact Mini vacuum former. There are many ways to design and manufacture vacuum forming molds. Surfaces generated from mathematical equations (e.g., with software like K3Dsurf) are simply controlled and easily varied by a small number of geometric parameters. 3D CAD (e.g., SolidWorks) offers an alternative for designing exoskeletons of shapes of greater complexity. The mold needs to be designed such that the plastic sheet, once formed, is removable. This is accomplished with either universal positive draft angle, or a multipart mold. Once the mold is design, a physical version can be constructed using a variety of techniques, each of which has associated trade-offs.

Molds of arbitrary geometry can be sculpted with clay (Fig. 12(*a*), Sculpey). This method is straightforward and low cost but is imprecise. Slice forms are an alternative that is also low in cost but more precise than clay. We used cardboard forms filled with polyurethane foam (Fig. 12(*b*), generated by Autodesk 123D). These two methods can be used to rapidly produce molds, and do not require any specialty equipment. They are most suited to creating proof-of-concept molds for low fidelity prototypes. Other methods can be used if more accuracy is needed. 3D printing (Fig. 12(*c*), printed with programable logic array (PLA) using an Ultimaker 2), is precise but also expensive and time consuming. Laser cut molds (Fig. 12(*d*), VersaLaser) are accurate but mostly limited to stacks of 2D shapes.

After the mold has been manufactured, it remains to select an appropriate polymer film to fabricate the shell structure. Many materials can be used, the only restrictions are that the polymer is a thermoplastic and that the film thickness is in a workable range. We have found good success with 760 μm thick polystyrene, 250–510 μm thick ABS, 130–250 μm thick polycarbonate, and 50–150 μm thick high density polyethylene. The former three materials are useful for structural shells, with polycarbonate having the largest flexural modulus (2.38 GPa) and the best forming of features that require large deformation of the formed material. Polyethylene is useful for forming flexible barriers against water and granular media.

After the mold is prepared and the material is selected, parts can be made with the vacuum-former. First, the plastic sheet is clamped to the frame of the vacuum-former, and heated by heating elements from above until it begins to sag (e.g., 230 °C, 30 s for 750 μm polystyrene, 25 s for 250 μm polycarbonate) (Fig. 11(*a*)). The heating elements are then removed, and the positive mold sitting on a stage underneath is quickly raised while a vacuum source is turned on. This results in cool air pressing the softened plastic sheet onto the mold and forming it into the shape of the mold (Fig. 11(*b*)). Finally, we trim away excess plastic at the base and smooth the edges to obtain the exoskeletal shell. In this way, complex integrated structures for robots can be rapidly produced.

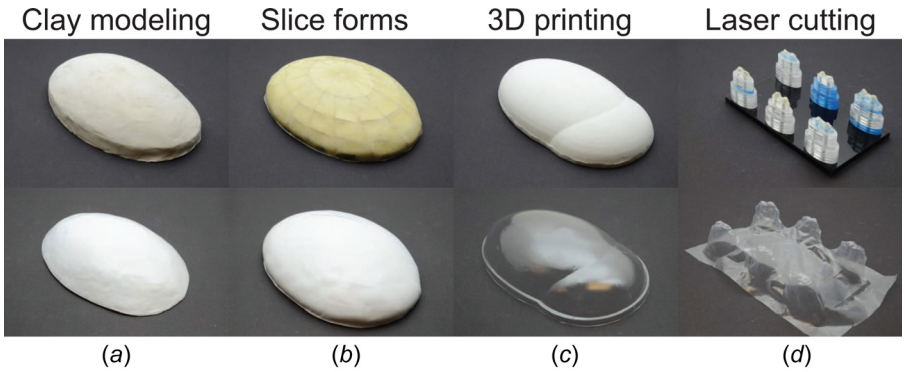

Fig. 12 Top: molds constructed using (*a*) clay modeling, (*b*) slice forms, (*c*) 3D printing, and (*d*) laser cutting. Bottom: exoskeleton shells made from these molds by thermoforming using ((*a*) and (*b*)) 750 μm polystyrene, (*c*) 250 μm polycarbonate, and (*d*) 50 μm polyethylene.

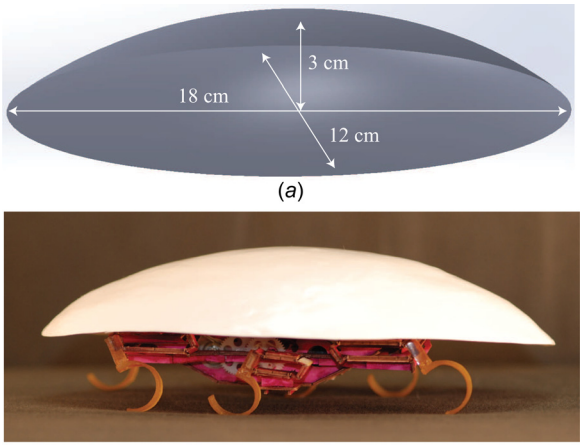

Fig. 13 Simple top shell for traversing cluttered terrain. (*a*) Design of shell shape resembling a thin slice of an ellipsoid. (*b*) Side view of VelociRoACH with the simple top shell.

5.3 Shells for Traversing Cluttered Terrain. A recent study has discovered that insects like discoid cockroaches have thin, rounded body shapes that assist their traversal through cluttered terrain such as grasslike beams, by facilitating passive body-rolling to align the smallest body dimensions with obstacle gaps (for more details of the animal experiments, see Ref. [40]). Inspired by this discovery, we designed and fabricated a simple top exoskeletal shell of similar shape to the cockroach to enable SCM robots to traverse similar cluttered terrain.

5.3.1 Design of the Traversal-Assisting Shell. This simple top shell is a thin slice of an ellipsoid, as shown in Fig. 13. It has similar overall aspect ratios (length:width:height = 6:4:1) to the exoskeleton of the discoid cockroach (7:3.5:1). It is slightly wider (relative to the animal) to fully enclose the perimeter of the VelociRoACH body. We hypothesized that maintaining shell shape is important in this application, so we chose 750 μm polystyrene sheets (McMaster) as a suitable material to create a relatively rigid shell.

5.3.2 Methods and Materials. A high-fidelity shell was not required for this proof of concept experiment, so the mold was fabricated with hand-sculpted clay (Sculpey). The clay mold was baked in an oven at 130 °C for 70 min, and polished to obtain a smooth surface. We fabricated a prototype shell by thermoforming a polystyrene sheet over the hand-sculpted mold, and then trimming it to size. The shell was mounted onto the robot using Velcro pads.

5.3.3 Characterization. To characterize the effectiveness of the exoskeletal shell in assisting cluttered terrain traversal, we challenged the robot to run though cluttered grasslike beam obstacles. With its original cuboidal body, VelociRoACH traversed with a 15% chance of success, even though the obstacle gap was wider than the robot body width. By contrast, VelociRoACH with the simple, rounded exoskeletal top shell passively rolled its body to the side in similar fashion as the cockroaches [40] and traversed the same cluttered terrain with a 90% success rate. Without any sensory feedback or changes in motor control, this integrated structure improved the VelociRoACH's ability to traverse cluttered terrain. While the shell adds significant weight to the robot (19 g shell weight vs. 26 g body weight), the robot's velocity does not decrease during running on open ground (60 cm/s with or without shell at 10 Hz). More details of the robot experimental setup, protocols, and results are described in Ref. [2].

Further, given the fabricated mold (~hours, ~$10), the cost in time (~minutes) and materials (~$1 per shell) for this shell fabrication process is significantly lower compared to existing techniques for navigation through cluttered environments, such as mapping and path planning. These techniques usually require additional sensors, computers, and actuators, and have long development and testing cycles. This makes the exoskeletal shell compatible with the low cost, dispensable applications of SCM robots.

5.4 Flexible Environmental Protection. For operation of SCM robots in potentially harmful environments, we want to add protection from water and granular media without limiting the motion of the robot. Flexible environmental protection also extends to protecting the environment from the robot for biomedical applications. However, we do not want to simply encapsulate the whole robot in a flexible layer because there needs to be an interface for the appendages to interact with the environment. For convenience, we also want the option to have the flexible shell be resealable.

5.4.1 Design of the Water Resistant Shell. We designed the flexible layer as a custom shaped "bag" made from high density polyethylene. This material has the benefits of being able to be formed on a thermoforming machine, and being able to be heat welded with a hand heat sealer (Audion Elektro). We assumed that the bag was inextensible and designed the bottom layer of the polyethylene bag to allow the robot mechanisms to move freely by adding the appropriate amount of slack. The geometry of the thermoformed bottom bag layer is shown in Fig. 14. An image of a robot leg passed through a protruding section of the bottom bag layer is shown in Fig. 15(*b*).

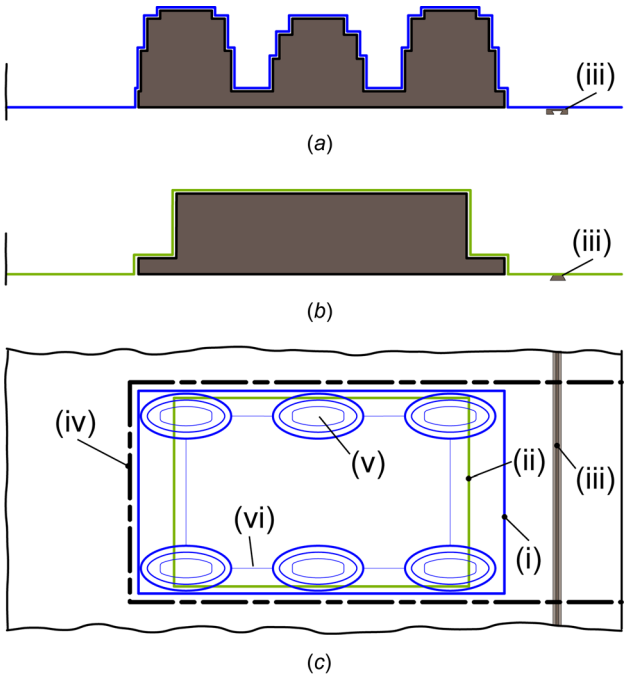

Fig. 14 Sealed bag layer manufacturing process. (*a*) Side view: forming of the bottom of bag layer with protrusions for freedom of leg motion; (*b*) side view: forming of the top of bag layer; (*c*) underside view: bag layer assembly with details (i) bottom piece of the bag, (ii) top piece of the bag, (iii) joining "ziploc" zipper on the bag, (iv) heat welds at the edge of the two layers, (v) formed out-of-plane pockets, shown topologically in this view, and (vi) extra vertical webs that form in the contoured bag layer between peaks, due to the high aspect ratio of the mold.

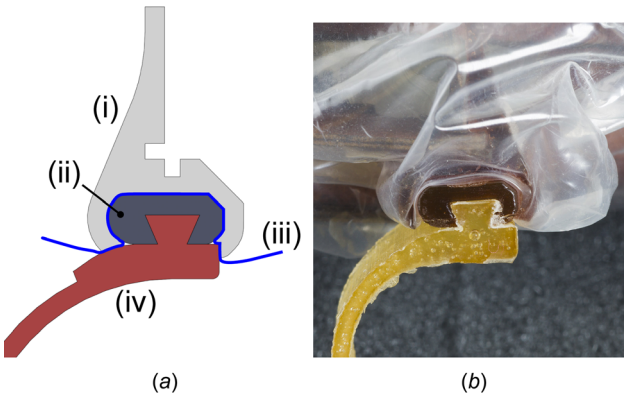

Fig. 15 Leg mounts that clip through the sealed bag layer: (*a*) diagram with details (i) half of the leg mount is attached to the robot hip inside the bag layer, (ii) the other half of the leg mount is outside the bag layer and snaps into the inner component, (iii) bag layer wedges between the two leg mount halves, (iv) VelociRoACH legs slide into dovetail connections on the outer component; and (*b*) close-up of molded leg clips capturing the sealing bag on the robot

There are several options to make the flexible layer resistant or impervious to the environment. If the robot needs to be waterproof, it can be fully heat sealed inside the bag. This approach precludes easy maintenance access to the robot. Water-resistant polyethylene zippers can be incorporated into the flexible layer to provide a reclosable seal against the environment, as shown in Fig. 19(*c*). This zipper leaks when submerged at depth in liquid, making the shielding merely water resistant, and not waterproof.

Our interface from the inside of the sealed bag is a two-part snap fit attachment. Half of the interface is attached to the robot hip inside the flexible bag layer. The other half is outside the bag layer and snaps into the inner piece, wedging the bag layer between the two components. A cross section of the cast polyurethane segmented leg mount that is designed for this purpose is shown in Fig. 15. Modular legs for the robot slide into dovetail connections on the outer components.

5.4.2 Methods and Materials. The process for manufacturing the flexible bag layer of the protective shell is shown in Fig. 14. The process begins by thermoforming protrusions into one side of a 51 μm thick split polyethylene zipper bag (Fig. 14(*a*)). Next, volume to accommodate the robot is thermoformed into the other side of the bag (Fig. 14(*b*)). Then, the zipper halves are joined and a hand heat sealer (Audion Elektro) is used to heat weld the three edges of the bag (welding through the zipper on the sides) and the bag is cut at the outer extent of the heat weld (Fig. 14(*c*)). The formed flexible bag layer protects the robot from water and granular terrain, is resealable, and allows for legged locomotion in conjunction with the leg mounts shown in Fig. 15.

5.4.3 Characterization. To test that the resealable polyethylene bag provides protection against the intrusion of granular media and water, VelociRoACH was inserted into the flexible bag layer and protective shell (following the procedure in Fig. 19) and run over both poppy seeds, and shallow water.

First, the robot ran for 5 min at full motor power through a 2.5 cm thick layer of poppy seeds. Approximately 6 g of poppy seeds accumulated in the structural shell of the robot, but no seeds were inside the polyethylene bag.

Next, VelociRoACH ran in place for 3 min a container filled to a height of 1 cm with water. The electronics and SCM mechanisms survived the test. However, some water droplets were observed inside the bag layer and there was some wetting of the lower cardboard structures. Upon inspection after the test, the bag layer appeared to have small perforations from the leg clips that allowed water to enter. From a separate evaluation of the zipper, it admits some water when submerged in shallow water, so it is another potential source of failure of the water seal.

To fully waterproof the robot we would omit the zipper and fully heat seal the robot into the bag. This comes at the cost of the re-usability of the bag layer. In addition, we would need to place shielding materials such as rubber or foam at any sharp interfaces that could potentially perforate the bag.

5.5 Protective Shell. The structural layer of the protective shell is designed to reduce the shock imparted to the robot by impacts while satisfying the constraints that it fits around the robot structure, and does not interfere with the motion of the legs.

5.5.1 Design of the Protective Shell. The protective shell is split into a bottom and top section that are thermoformed separately. The top shell (shown in Fig. 16) is designed such that it does not interfere with the VelociRoACH's SCM linkages. This leaves the design space mostly open. We chose an ellipsoidal shell shape that we expect to enable the higher order locomotory capabilities described in Sec. 5.3 while being capable of absorbing impact from high-speed collisions.

Shown in Fig. 16, a kinematic model of the VelociRoACH transmission was used to trace out the trajectories of the leg tips of the robot. These trajectories are used in conjunction with the solid model geometry to shape the shell volume such that there is no interference of any mechanisms or leg with the shell. During this process, a secondary ellipsoidal bulb was added to the front shell volume in order to clear the forward part of the front leg stroke. The top shell also needs an interface to the bottom shell. We chose to use an integrated snap-fit ring along the bottom edge of the top shell. This approach has the advantage that it is reclosable, and requires no adhesives. On the top shell, this feature is

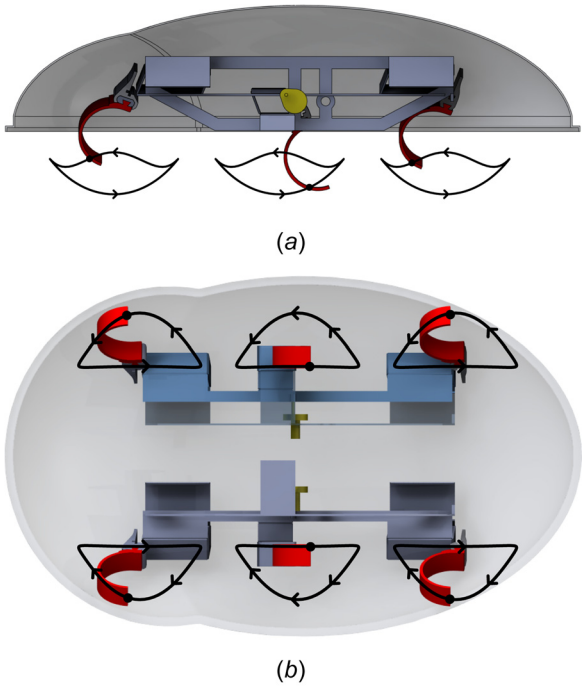

Fig. 16 (*a*) Side view and (*b*) underside view of solid model renderings of VelociRoACH assembled in the structural shell. The structural shell clears the leg motion of the robot.

accomplished with an outwardly protruding lip which is shown in Fig. 16.

Shown in Fig. 18, the bottom shell requires more complicated geometry than the top shell. It incorporates an undercut lip which retains the protruding lip of the top shell. It also has material cut away to allow pass-through of the legs. The bottom shell was designed to have these features be cuttable with an infrared laser. The limited focal range of the laser cutter limits the curvature of the bottom shell, so it must be mostly flat.

The primary function of the thermoformed protective shell is to mitigate impact shock. Therefore, after designing the shape of a structural shell to fit the form and kinematics of the robot, the stiffness of the shell needs to be tuned to absorb impacts. Assuming a linear cantilever beam model of the shell and no rebound after hitting the ground, the peak impact acceleration felt by the robot after a drop is given in Eq. (1)

$$a_{\max} = \sqrt{\frac{Ebt^3gh}{12mL^3}} \tag{1}$$

where E is the Young's modulus of the shell material, b is the overall width of the shell structure, t is the shell thickness, g is acceleration due to gravity, h is drop height, m is total mass, and L is the overall length of the shell structure. If we assume that b, L, and m are set by the robot in the exoskeleton, then E and t are the design parameters to adjust the shell stiffness to bring the impact acceleration below a target value. The elastic moduli of thermoformable polymers are largely constant, and prescribing the stiffness of the shell by material choice limits the design space. A material of the right stiffness may have suboptimal attributes in other areas, such as impact resistance, formability, or laser machine-ability. We chose polycarbonate for the shell because it excels in these areas and we tuned the shell's stiffness with geometric design.

With the material fixed, tuning the shell thickness t is an effective way to minimize the impact acceleration, because the peak acceleration $a_{\max}$ scales with $t^{3/2}$. Additional considerations that need to be made when adjusting shell thickness are that the added mass of the shell increases linearly with t, and the shell may bottom out against the robot body during impact if it falls below a stiffness threshold, which can increase the peak impact acceleration. Another option to increase stiffness is by adding structural ribs to the top and bottom shells.

5.5.2 Methods and Materials. The top shell mold was made with a 3D printer (Ultimaker 2) because of the precision required for the outwardly protruding lip that snaps into the receiver lip on the bottom shell. The 3D printed mold is made of PLA plastic with a 3 mm hull that is filled at a 30% volume rate. This build setting produced an excessively strong mold, and the hull thickness and fill rate could be reduced to reduce build time. A diagram of a thermoformed top structural shell is shown in Fig. 17. polycarbonate of 250 μm sheet thickness was heated for 25 s before being formed over the top mold.

The bottom structural shell manufacturing process is shown in Fig. 18. The overhead and cross section diagrams of the thermoformed bottom shell (Figs. 18(*a*) and 18(*b*)) show the structural ribs, vacuum feeds, undercut lip, and alignment pins in the mold. Because the bottom shell is largely planar, all three layers of the mold are made of laser cut acrylic; the base and middle layers are 6.35 mm thick and the top layer is 3.18 mm thick. The base layer of the mold contains laser etched channels (raster, 80% power, 12% speed) that are approximately 1.6 mm deep. When the polycarbonate is formed over the mold, the channels form stiffening ribs into shell. As a general process guideline, the width of the ribs should be at least twice their depth in order to fully form. Vacuum feeds are cut through the base layer around the outermost edge and along the center of the rib trenches in order to sufficiently form the undercut lip and rib features. The vacuum feeds are cut without forming any closed curves to ensure the base mold layer remains a single piece. The middle layer of the mold defines the outer extent of the undercut lip and stacks over and aligns to the base layer using 3.18 mm diameter aluminum alignment pins that are anchored in the base layer. The top layer of the mold defines the inner extent of the undercut lip and is placed over the middle layer using the same alignment pins. The middle and top plates are split along a line of symmetry to release the shell after forming.

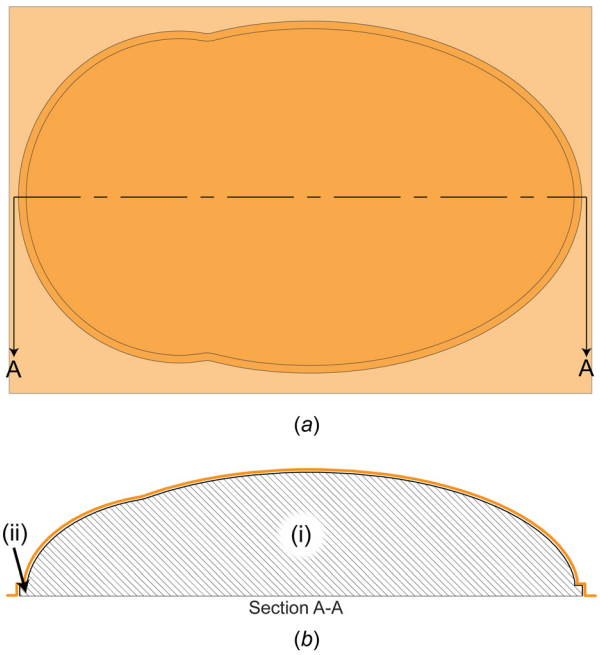

Fig. 17 (*a*) Top view and (*b*) side section view of the thermoformed structural top shell over a 3D printed mold. (i) 3D printed PLA plastic buck with a 3 mm hull and 30% fill. (ii) Outwardly protruding lip at the base.

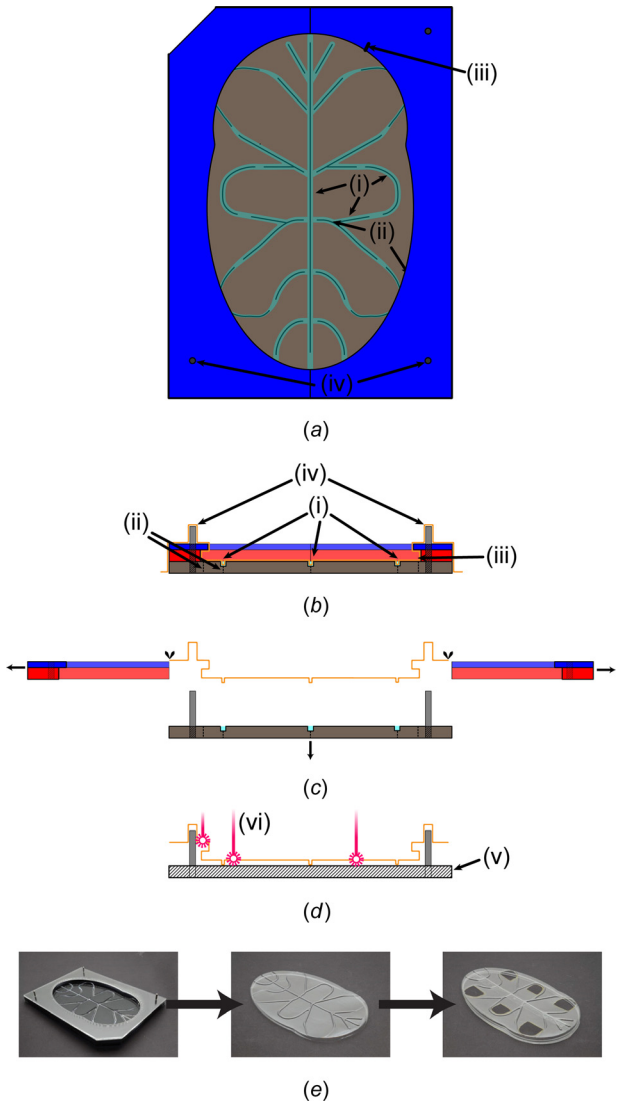

Fig. 18 Bottom structural shell manufacturing process: (*a*) overhead view of multilayer laser cut mold. The pattern in the bottom layer will form the structural ribs (i), and thin cuts provide vacuum feed (ii). The top plate of the mold forms the undercut lip feature (iii). Alignment pins (iv) are added to stack up the mold layers. (*b*) Cross section view of thermoformed plastic shell in mold, where the undercut lip (iii) formed by separate layers of the mold is shown. (*c*) To release the formed shell, the shell is roughly cut around the top layer of the mold, the base plate with dowel pins is pulled downward and the top two plates defining the undercut lip are pulled outward. (*d*) The roughly cut shell is aligned to a fixture plate (v) for the laser cutting which duplicates the alignment pin pattern as in the stack-up above, and then holes for legs and final outline release cuts are made by the laser (vi). (*e*) Images of the bottom shell mold, thermoformed bottom shell, and finished bottom shell after release cuts.

The bottom shell is made by thermoforming the 250 μm polycarbonate sheet into the bottom mold using the same process time as for the top shell. The uncut bottom shell is released from the mold (Fig. 18(*c*)) by roughly cutting around the top layer of the mold outward of the alignment pins, pulling the base plate with dowel pins downward, and then pulling the middle and top plates outward along their parting line.

As a final process step, the roughly cut bottom shell is precisely cut using a laser cutter (Fig. 18(*d*)). The parts of the bottom shell that were thermoformed over the protruding alignment pins are snapped over alignment pins in a matching laser cutting jig plate.

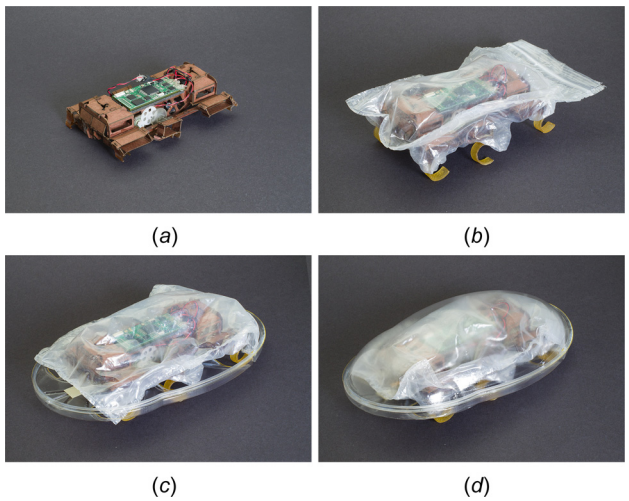

Fig. 19 Assembly process for adding shell to the robot: (*a*) cardboard robot body; (*b*) with PE bag and mounted legs; (*c*) with bottom structural shells; and (*d*) complete with top structural shell

With the top left corner of the jig plate as a coordinate reference in the laser bed, the laser cutter is used to cut outlines around the receiver lip and the through holes for the legs. The laser is focused to the flat top layer of the formed shell. The cut settings for the leg holes (10% power, 2.5% speed) are twice the power of those used for the receiver lip (5% power, 2.5% speed) because the bottom of the shell is not fully in the range of focus for the laser. Images of the bottom shell mold, thermoformed shell before precise cuts, and final bottom shell after precise cuts are shown in Fig. 18(*e*).

We show assembly of a VelociRoACH with the protective shell and sealing layer from Sec. 5.4 in Fig. 19. Each assembly step is reversible by design, so that it is possible remove the robot from the shell for maintenance. Assembly order begins with the folded cardboard robot chassis as shown in Fig. 19(*a*), with actuators and control board installed, and molded leg clip receivers at the leg roots. In Fig. 19(*b*), the body is inserted into the flexible bag described in Sec. 5.4, which is then sealed at the anterior with the "ziploc" strip bonded into the bag. The legs are clipped onto the leg clip receivers through the bag layer as detailed in Fig. 15. In Fig. 19(*c*), the bottom structural outer shell element is adhered to the underside of the sealing bag and, in Fig. 19(*d*), the top shell piece is snapped into the rim feature of the bottom shell.

5.5.3 Characterization. As an evaluation of the protective shell, the robot was assembled in the shell following the steps in Fig. 19 and dropped from various heights. After initial tests demonstrated structural damage to the robot and the failure of the snap fit between the top and bottom shells from drop heights as low as 3 m, a layer of foam (1.6 g) was added between the top of the robot and the top shell. With the addition of this shock absorbing component, the robot and shell assembly remained undamaged and intact after two successive drops from four stories with a top-first impact orientation.[7] The SCM structures, transmissions, and electronics of the robot sustained no damage. Also, the snap fits of the segmented leg mounts and structural shell remained secured in place after the drops. However, the battery connection was lost upon impact and after bouncing, the robot did not land on its feet in one of the trials.

Although the protective shell offers improvements in locomotion over granular media and impact resistance, it also comes at some cost. VelociRoACH in the protective shell could run on flat carpet at 1.1 m/s, which is 40.7% of the top speed of the

[7]The robot in the shell preferentially falls top first due to aerodynamic effects.

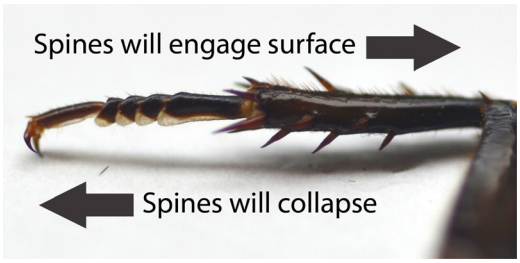

Fig. 20 Cockroach (*B. discoidalis*) leg spines. Arrows indicate the direction of the force applied to the spines.

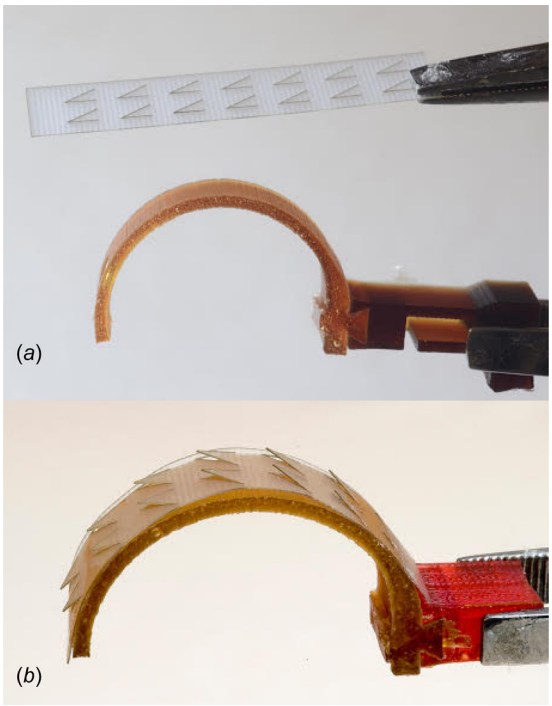

Fig. 21 Process to create the claws. Figures (*a*) and (*b*) are pictures of the fabricated components. To make the legs, the outline of the claws was first laser-cut into a rectangle of fiberglass. (*a*) Then the fiberglass was glued onto a curved leg. (*b*) Claws stick out because the fiberglass remains flat in the released sections.

unencumbered robot [11]. The shell adds a total of 13.5 g of mass (10.7 g structural layer, 2.7 g bag layer) to the 30.1 g robot (with battery and board). Also, the shell increases the length by width by height dimensions of the robot from 10 cm × 7 cm × 4.5 cm to 18.5 cm × 12 cm × 5.3 cm.

6 Claws

Numerous robots have used claws to climb walls [14,41,42] or walk over adverse terrain [1]. These claws were inspired by anisotropic spines found on the legs of cockroaches and arthropods [1], shown in Fig. 20. In this section, we present a method to rapidly fabricate arrays of anisotropic claws.

6.1 Methods and Materials. The claws are made by cutting triangles with an inner angle of 45 deg into 125 μm thick fiberglass sheet with a UV laser (PMI) as shown in Fig. 21. This shape allows for anisotropic engagement forces which allow the robot to lift its leg off the ground more freely. After the claws have been cut they are mounted onto the curved legs of the robot, at which point the claws are revealed as shown in Fig. 21. The claws are

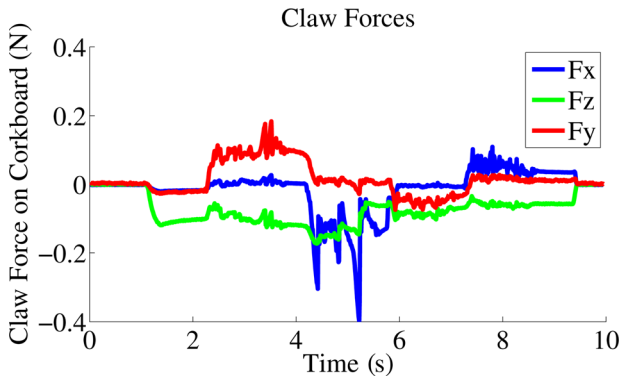

Fig. 22 Plot of the forces exerted by the claw onto a test substrate as it is pulled in the F_x and F_y directions and preloaded with F_z. Fy indicates the fore-aft forces while F_x shows lateral forces.

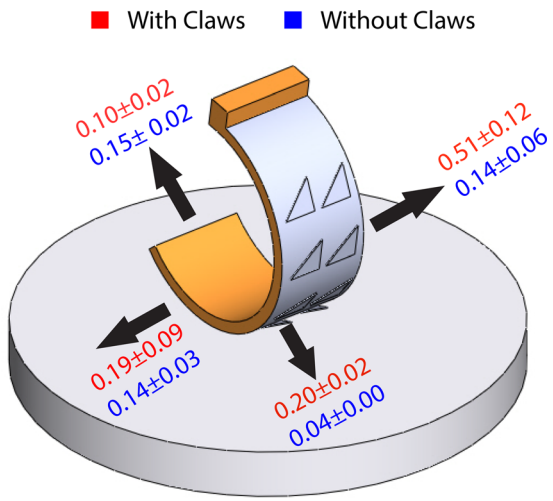

Fig. 23 The forces required to disengage the spines from a piece of corkboard. The arrows indicate the disengagement force's direction.

adhered so that the sloped edge of the triangle is always on the outer side of the robot.

6.2 Characterization. Load-drag-pull tests were performed in the fore-aft and lateral directions on a robot leg with integrated claws. The recorded force profile (Fig. 22) shows the normal loading force F_z, the fore-aft force F_y, and the lateral force F_x. A load of 0.2 N is required to disengage the corkboard while the claws are penetrating the surface. The claws can be released with a force of 0.1 N, for a 2:1 ratio between holding and releasing force (Fig. 23). Less force was required to disengage the foot in the direction of the sloped edge, as compared to the side with a straight edge. To evaluate their utility on a robotic platform, the claws were mounted to a VelociRoACH, a hexapedal terrestrial robot [11], to test functionality. This work is described in a future paper.

7 Tactile Sensors for SCM Robots

Legged SCM millirobots can operate in rough terrain, confined spaces and in the presence of obstacles such as foliage. To operate effectively in such difficult and uncertain environments, tactile sensory feedback from surfaces with which they interact is useful. Two SCM-compatible tactile sensors were developed to provide such information. The first is a binary, hair-based sensor array, which uses bio-inspired polymer hairs to detect both normal and

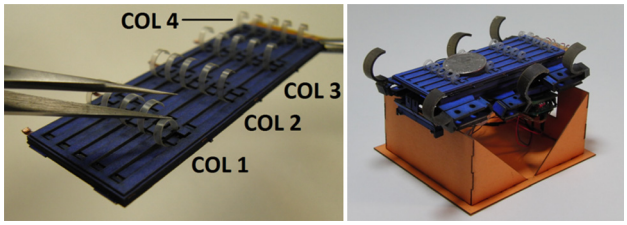

Fig. 24 (Left) 5 × 4 array of binary hair sensors. (Right) Hair sensor array mounted to bottom of hexapedal SCM robot [43].

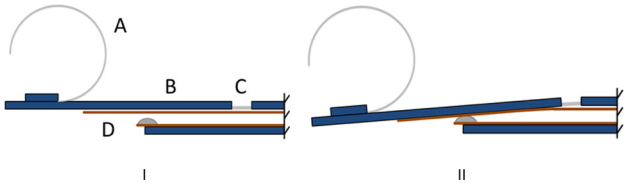

Fig. 25 Hair-activated switch in open (top) and closed (bottom) configurations. Sensor consists of curled polymer hair (A), rigid lever arm (B), polymer flexure (C), and copper contacts (D) [43].

shear contact forces. The second is an analog tactile bumper capable of measuring contact forces when bumping into obstacles.

7.1 Binary Hair Array. A 5 × 4 binary hair sensor array[8] was developed to provide SCM robots with the ability to detect contact with ground obstacles (Fig. 24). The sensor consists of an array of highly sensitive binary contact switches, where each switch is activated by a compliant polymer hair originating from the tip of the switch. The sensor can be fabricated using an entirely laminar roll-to-roll process that is compatible with the SCM fabrication methodology.

Each hair sensor consists of a lever arm (B) of rigid structural material hinged at one end through a polymer flexure (C). The sensor array discussed here uses four-ply cardboard (0.4 mm thick) as the structural material and 75 μm-thick PET film for the flexure hinges. Curled polymer hairs (A) are held in place at the tip of each switch lever by small blocks of cardboard that, together with adhesive, adhere the roots of the hairs to the lever tips. When the hairs are perturbed, either through normal or shear contact forces, the levers deflect downward, pivoting at their flexure hinges, bringing two copper layers (D) into contact. (Fig. 25)

7.1.1 Manufacturing. A key design feature of the hair sensor array is that it can be fabricated using an entirely laminar process, in which the full sensor is assembled by stacking up layers of material via lamination, while forming the required mechanical features on the accumulating stack-up using a laser-cutter. Overall, the hair sensor array is the product of 13 separate layers that stack together to form the electrical contacts, switch levers and hairs (Fig. 26). The curled hairs are formed by laminating a precurled film composite consisting of 25 μm polypropylene (PP) laminated together with 50 μm low-density polyethylene (LDPE). When laminated at a temperature of 177 °C and a pressure of 345 kPa, the two polymer films fuse together to form a composite with a natural radius of curvature of 3–4 mm.

7.1.2 Characterization. The average sensitivity of the hair-switches in the array was characterized by determining the minimum threshold weight at which different sized patches of hairs become active. Here, a patch of hairs was labeled as active if at least 2/3 of the loaded hairs were active. The results are plotted in Fig. 27. The dashed trend line is the least-squares fit (zero intercept) to the data points, indicating an average normal sensitivity of 0.79 g/hair.

[8]Some of the information presented for the binary hair array is a refinement of work that was previously presented at a conference [43].

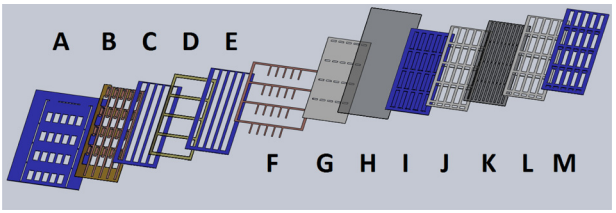

Fig. 26 Layers that comprise the hair sensor array: (A) base layer, (B) bottom contacts, (C) spacer, (D) insulating polymer film, (E) spacer (F), top contacts, (G) paper backing, (H) flexure polymer film, (I) switch levers, (J) precut sheet adhesive, (K) prestressed hair film (L), precut sheet adhesive, and (M) hair mounting layer [43]

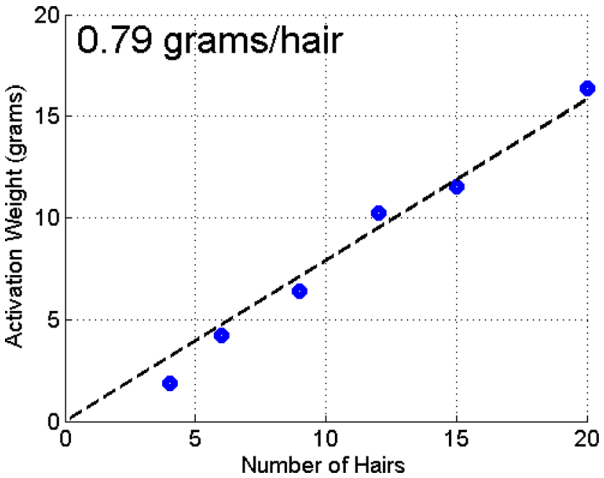

Fig. 27 Total loading required for sensor activation as a function of the number of hairs loaded [43]

7.2 Force-Sensing Taxel Array. To complement the contact sensor array, an analog force-sensing taxel array was developed for measuring the magnitude of contact forces. The analog tactile sensor consists of an array of rapidly manufactured force-sensing elements, arranged on a cylindrical bumper structure that attaches to the front of a legged millirobot (Fig. 28).

The tactile bumper consists of a 2 × 7 array of force-sensing taxels attached to the front of the hexapedal millirobot through a cardboard mounting structure. Each taxel consists of a reflective Mylar-film patch supported on foam walls above a Sharp GP2S60 proximity sensor (Fig. 29). The force-sensing taxels are designed to exhibit two sensitivity regions, meaning that they have greater sensitivity at small deformation, to detect smaller contact forces, and then become less sensitive at larger deformation, to increase the saturation force.

7.2.1 Manufacturing. The foam sensory structures that sit above the array of proximity sensors are formed through a laminar process involving the incremental build-up of features through lamination and laser cutting (Fig. 30). To begin, a patterned layer of sheet adhesive is laminated to a cardboard base, and regions of the adhesive are exposed by scoring via laser, and removing portions of the paper backing. The exposed adhesive regions are used to anchor down 2.6 mm thick inner foam wall features. Taller, outer foam walls are formed by laminating an approximately 3.2 mm thick patterned foam sheet to a 50 μm thick reflective Mylar-film, and then laminating the foam–Mylar stack-up to the base layer. Individual taxel structures are isolated from one another by

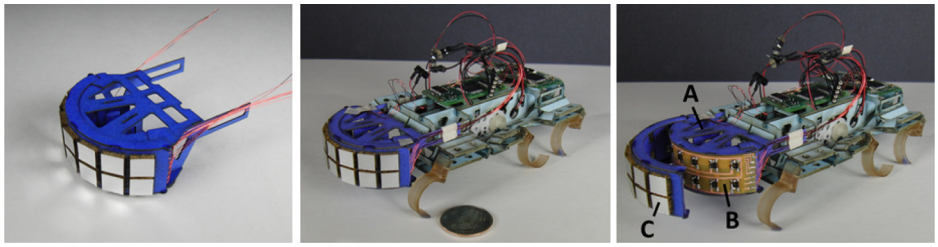

Fig. 28 (Left) Force-sensing taxel array. (Center) Bumper attached to front of hexapedal SCM robot. (Right) Three subcomponents of bumper: cardboard mounting structure (A), array of proximity sensors on flex-circuit (B), and outer layer of foam sensory structures (C).

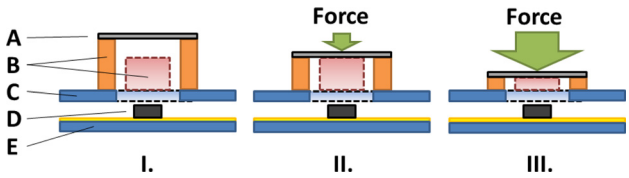

Fig. 29 Cross section illustration of force-sensing bumper taxel. Taxel structure consists of 50 μm thick reflective Mylar-film (A), outer and inner urethane foam walls (B), foam-supporting cardboard layer (C), sharp GP2S60 proximity sensor on flex circuit (D), and bumper mounting structure (E).

laser-cutting their outlines into the Mylar and foam and peeling away the excess material left in between.

7.2.2 Characterization. To characterize the sensitivity of the foam taxel structures, the response of a single taxel was recorded over a range of statically applied loads and displacements. These data were combined using the response-to-load data as a calibration for estimating the forces corresponding to the applied displacements. The result is the sensitivity characterization curve shown in Fig. 31, which highlights the dual-sensitivity of the foam taxels.

8 Legs With Integrated Load Sensing

The ability to estimate applied forces in either biological or robotic systems is useful, with direct applications in manipulation, optimal control, and estimating contact interactions with nonrigid objects. To this end, we developed a process to create fiberglass robotic appendages with flexible, piezoresistive strain gauges that are fabricated in situ (Fig. 32).

Compact, flexible piezoresistive sensors have been developed for high-sensitivity strain measurements by Takei et al. [44]. The sensors consist of a particle desorption mass spectrometry (PDMS) substrate with a printed strain-sensitive CNT/silver nanoparticle (CNT-AgNP) composite ink coating. The strain sensors

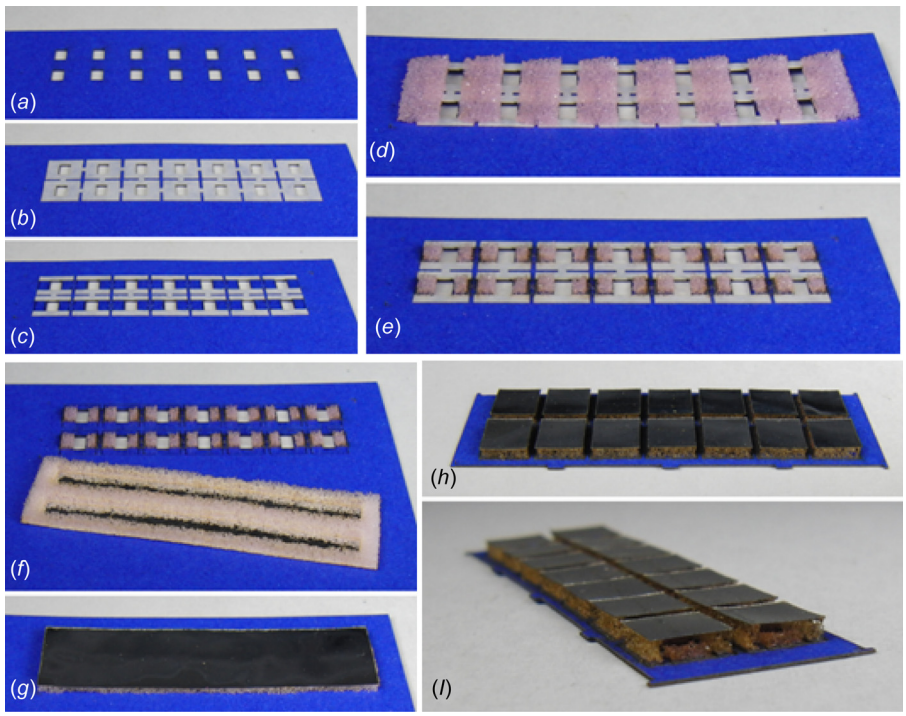

Fig. 30 Laminar fabrication of sensory foam structures: Patterned cardboard base for foam structures (*a*), patterned sheet adhesive laminated over base (*b*), regions of adhesive exposed for anchoring inner foam walls (*c*), foam strips laminated down onto exposed adhesive regions (*d*), inner foam walls laser-cut from foam strips (*e*), taller, patterned foam laminated onto reflective Mylar-film (*f*), taller foam laminated onto base (*g*), and foam structures are isolated by cutting through Mylar-film and underlying foam, but not cardboard base, and peeling away excess material ((*h*) and (*i*))

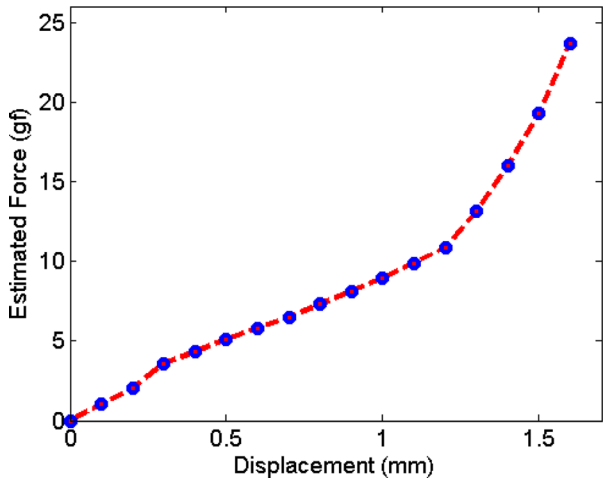

Fig. 31 Estimated force versus applied displacement for single taxel

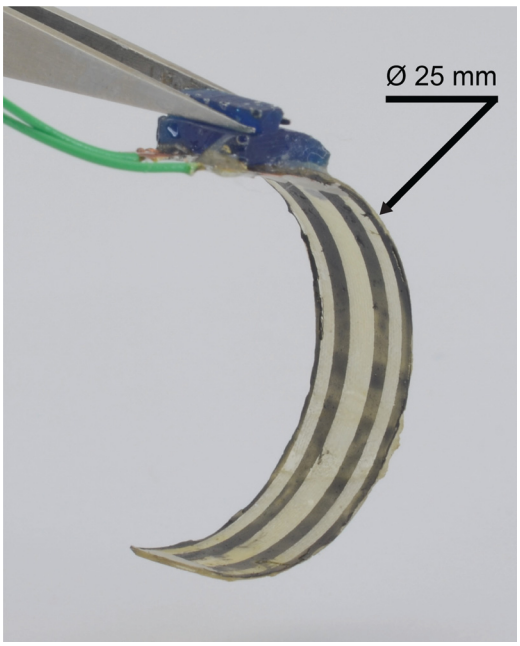

Fig. 32 Fiberglass robot appendage with integrated CNT-AgNP piezoresistive sensor (black traces)

have been shown to operate with a gauge factor of ~95 and at strains of ±2% for hundreds of cycles without degradation.

Improvements on the process from Takei et al. [44] enable these CNT-AgNP strain gauges to be manufactured in situ, as we demonstrate here on a set of curved fiberglass C-legs used by our hexapedal SCM robots. This process produces strain gauges that operate with approximately zero initial strain on surfaces of any geometry to which a template can be applied.

These gauges contrast with conventional strain gauges, which are manufactured flat and must be bent onto a curved C-leg—introducing sensor strain even when the leg is in a zero-strain configuration. Depending on the strain gauge thickness/sensitivity and the substrate radius of curvature, this initial strain can cause saturation of the strain gauge—typical gauges saturate at ~0.5% for semiconductor gauges and ~3% for metal foil gauges. These strain gauges are also difficult to apply, requiring accurate and reliable surface pretreatment and bonding operations.

8.1 Methods and Materials. The manufacturing process is shown in Fig. 33. The piezoresistive sensors were fabricated

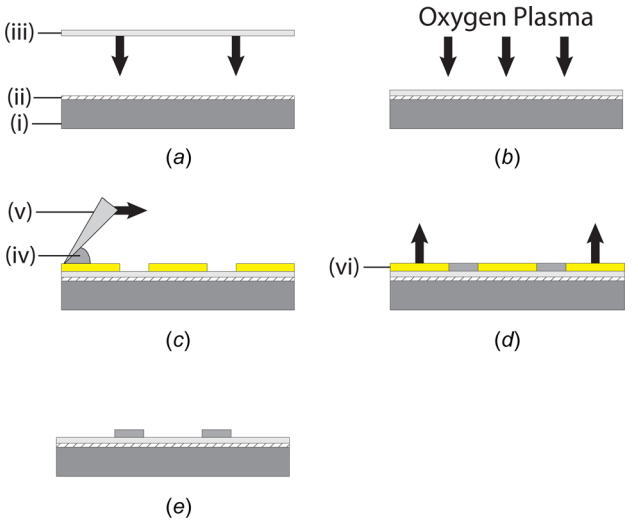

Fig. 33 Manufacturing process for the strain sensor: (*a*) fiberglass leg substrate (i) is sequentially covered with a sheet of 3M 468MP tape (ii) and a sheet of PDMS (iii); (*b*) oxygen plasma etch; (*c*) PET mask (vi) is aligned and a uniform layer of the CNT-AgNP ink (iv) is applied with a spatula (v); (*d*) ink dries at ambient conditions and the mask is removed; and (*e*) ink baked/annealed in an oven

directly on a set of fiberglass robot legs, and are composed of a flexible sheet—PDMS (Dow Corning Sylgard 184)—with a patterned ink electrode—CNT ink (SWeNT V2V Ink) and AgNP ink (Paru Co. Nano Silver Ink) composite.

The CNT-AgNP ink composite used had a composition of 95 wt.% CNT ink and 5 wt.% AgNP ink. Ink compositions with 30 wt.%, 5 wt.%, 1 wt.%, and 0 wt.% AgNP were tested. Inks with higher concentrations of AgNP ink had increased piezoresistive sensitivity, but degraded (film cracking) due to fatigue and overloading more easily. 5 wt.% AgNP ink yielded the best balance of device sensitivity and robustness.

The fiberglass legs and PDMS sheets were batch-manufactured. The fiberglass legs were formed as a semicircular sheet with a radius of 12.5 mm and thickness of 250 μm (8 layers of fiberglass sheet), and individually cut to a width of 7.25 mm. The PDMS sheets were manufactured in 7.25 mm × 45 mm × 50 μm sections by pouring uncured PDMS in a laser-cut PET template (50 μm thick), leveling, and curing (125 °C for 20 min).

The concave side of the fiberglass legs were then sanded, wiped clean, and covered with double-sided acrylic adhesive tape (*3M* 468MP, 132 μm thick). A thin, uniform layer of uncured PDMS was applied to the tape. The cured PDMS sheets were placed on the tape/uncured PDMS, and these assemblies were cured (125 °C for 20 min). The leg assemblies then underwent an O_2 plasma surface etch[9] for 2 min (with the PDMS sheets aligned toward the plasma source).

A PET mask (25 μm thick), laser-cut with the desired electrode pattern, was aligned and pressed onto the PDMS substrate. The CNT-AgNP ink was then applied over the mask and leveled with a metal spatula. The ink was partially dried (room temperature for 10 min), the PET mask was removed, and the ink was fully cured/annealed (70 °C for 60 min).

Two strips of copper foil tape (*3M* 1181) were secured on the leg adjacent to the terminals of the CNT-AgNP ink trace, electrically connected with a layer of silver ink (DuPont 5025), and the ink was cured (70 °C for 60 min). Leads were soldered to the copper tape for resistance measurements.

[9]O_2 plasma etchers cost approx. $10,000 USD (e.g. SPI Plasma Prep III), or machine time can be rented in many microfabrication facilities.

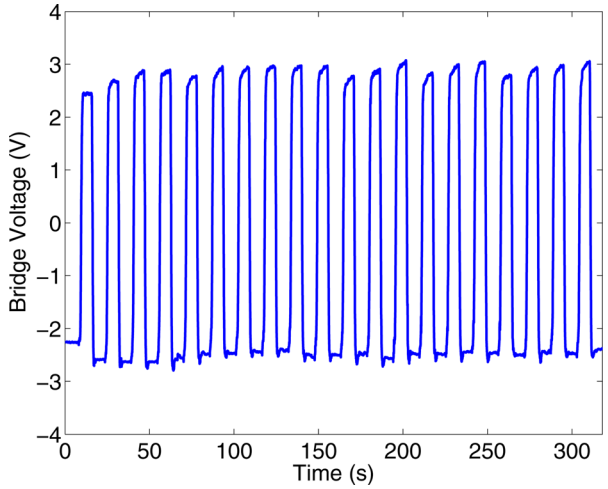

Fig. 34 Amplified bridge voltage (V) for the strain gauge as a function of time (s). Data is presented for 20 loading/unloading cycles to an applied uniaxial compressive force of approximately 25 mN (uniaxial compression of 6.0 mm).

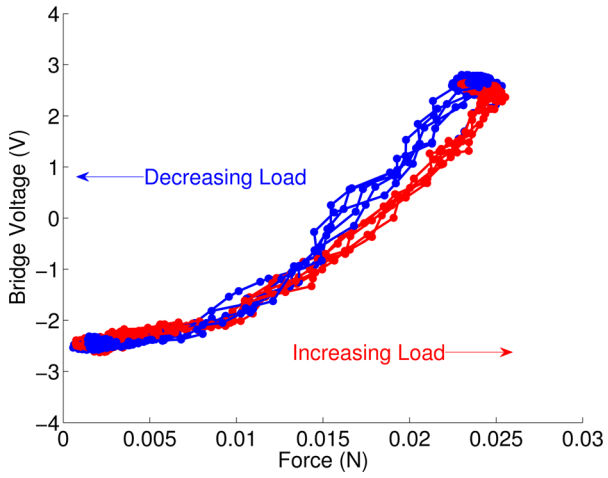

Fig. 35 Amplified bridge voltage (V) versus applied uniaxial compressive force (N) for the strain sensor. Data is presented for 5 consecutive loading (red)/unloading (blue) cycles.

8.2 Results. The piezoresistive properties of the strain gauges were characterized by placing individual legs in compressive, uniaxial loading up to ~25 mN (6.0 mm of compression on a leg with 25 mm diameter). The loading force was measured by a six-axis force/torque sensor (ATI Nano43), and changes in the strain gauge resistance were monitored using a Wheatstone bridge and signal conditioning amplifier (Techkor MEPTS-9000) to yield an output voltage (referred to hereafter as the bridge voltage).

The results of cyclic loading are highlighted in Fig. 34, which presents data from the first 20 cycles of a 50 cycle test. Repeatable performance was observed: the mean change in bridge voltage (from unloaded to loaded states) is 5.21 V with a standard deviation of 0.13 V, and there is no correlation in the deviations of this bridge voltage variance across the 50 cycles. Minimal sensor degradation was observed after more than 300 cycles of testing.

The relationship between applied load and the amplified bridge voltage is shown in Figs. 35 and 36, and can be modeled with a quadratic function ($R^2 = 0.997$)

$$V_{\text{Bridge}} = (1.13 \times 10^4)\,(F - 3.12 \times 10^{-3})^2 - 2.47$$

The sensor provides reliable sensitivity to compressive loads of up to approx. 24 mN. The bandwidth of the sensor was estimated to be 3.4 Hz (using system identification to fit a 2-pole, 1-zero

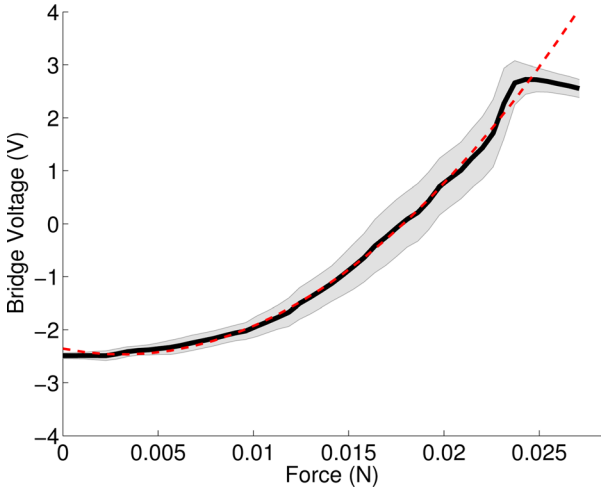

Fig. 36 Amplified bridge voltage (V) versus applied uniaxial compressive force (N) for the strain sensor. Data average (black) with $\pm\sigma$ (gray regions) is presented for 50 consecutive loading/unloading cycles. The sensor provides reliable sensitivity to compressive loads of 0 to ~24 mN and saturates for loads above this. A quadratic regression function (red dash) was fit to the data for sensor calibration.

transfer function to this same dataset). The time lag between the applied load rise time to 90% of F_{Max} and the bridge voltage rise time to 90% of V_{Max} was measured as a mean of 0.29 s with a standard deviation of 0.096 s (for six randomly selected cycles). The speed of the motion stages on our force sensing platform was limited to 3.3 mm/s, so these numbers represent a lower bound on the bandwidth of the sensor.

It should also be noted that the current manufacturing process (manual ink deposition) introduces variability in the CNT-AgNP trace resistance. A batch of five sensor legs manufactured with identical masks had a mean unstrained resistance of 3.38 kΩ with a standard deviation of 1.61 kΩ.

Of these five legs, four legs were tested with one of two coatings, with the intention of sealing the traces to reduce abrasion/degradation. Both coatings affected the sensitivity of the sensors. Coating the full leg assembly with Parylene (1 μm) eliminated all measurable strain sensitivity. Covering the leg assembly with VHB tape (*3M* VHB Tape, 250 μm thick) increased the sensor saturation load to ~37 mN, but produced a deadband for loads below ~20 mN. The deadband was characterized by a notable viscoelastic effect (particularly on the decreasing load trajectories): the sensor resistance/voltage decreased for loads between the unloaded (~0 mN) state and ~20 mN. This behavior is likely caused by residual stress in the VHB tape, but further testing is required to confirm this.

For the VelociRoACH, loading on an individual leg can be expected to range from ~0–400 mN during locomotion. The current sensor is thus capable of measuring low loading phases (leg lift-off, aerial, and touch-down) where the legs are intermittently in contact with the ground and lightly weighted. Sensor saturation currently prevents measurements in higher loading phases that exceed 24 mN. VelociRoACH legs, however, are designed with a stiffness of approximately 40 N/m [11], whereas the legs with integrated strain sensors had a stiffness of only 3.2 N/m. Future manufacturing of these strain sensors on legs of appropriate stiffness, should yield devices capable of measuring a larger range of loads.

9 Conclusions

In this work, we presented methods to design and fabricate folded robots, protective structures, traction enhancing elements, reel-to-reel compatible force sensing arrays, and paintable,

Table 3 Contributions

Section	Contribution	Functionality	Process advances	
			Cost	Time
3: Materials	New core material for SCM	Crush strength improved 780 → 3350 g	+	+
4: DFM	Self-fixture and reflow process	Assembly time reduced 3 hr → 20 min	0	−−
5: Shells	New protective structures	Robot survives 4-story falls, is water resistant	+	+
6: Claws	Rapid-fabricated arrays of claws	Capacity for traction generation doubled	−−	−−
7: Tactile arrays	Reel-to-reel force sensors	New taxel array senses applied forces	+	+
8: Ag-CNT sensor	Flexible, in situ strain gauge	Strain gauge bandwidth at least 3.4 Hz	−	+

flexible force sensors. All of these elements are compatible with low-cost folded robots, and could be integrated in various combinations depending on the particular task. The contributions of this work have been summarized in Table 3. +/−/0 correspond to increasing/decreasing/constant changes in fabrication cost and time.

Design files for an open-source robot, the OpenRoACH have been released with this publication. A self-fixture and reflow process which was presented in Sec. 3 reduced the assembly time for the SCM based VelociRoACH from 3 hr to 20 min. An additional benefit was that the robotic platform was made more robust. The reflow process causes the thermal adhesive to penetrate deeply into the cardboard, reinforcing the tabbed connections. In a stress test, these joints withstood ten times the load of a traditional (folded and glued) joint before failing.

The templating step is currently done by hand, and is being replaced with a 3D printer which accurately deposits the glue. This process allows for the rapid assembly SCM robots in the tens of grams scale. It is also amenable for mass-produced field assemblable robotic structures because it is reel-to-reel compatible and furthermore needs only a heat source for assembly. The integrated nature of SCM components enables the creation of highly capable robots from affordable materials. The presented assembly method allows those robots to be created more quickly.

We identified materials which are appropriate for larger-scale folded robots. A composite made with balsa wood and copy paper reinforced with cyano-acrylate adhesive was the stiffest and strongest of the tested materials. An OpenRoACH built with this material withstood over four times the load withstood by a robot of identical design which was made from cardboard. Increasing the stiffness and strength of SCM materials increases the flexibility of SCM robot designs. CAD for SCM structures is easily scaled; by using stiffer materials, no additional reinforcing structure needs to be added to the design of larger versions of the same robot. We confirmed that GFRP is a good material to make strong SCM components, if the toxic products from its cutting can be dealt with. Ripstop nylon was presented as a suitable flexure material for robust SCM robots.

In Sec. 5, we gave details on how thermoforming can be used to produce protective exoskeletal structures for robots. A thermoformed part takes ∼30 s to mold; after molding, these parts can be cut with a laser trimming process which takes less than 60 s. These protective structures were shown to have a variety of functions. A shell that assists open-loop navigation of cluttered terrain was shown. We also demonstrated the design and construction of a multimaterial protective shell integrated into the VelociRoACH. When compared to the simple shell for navigating cluttered terrain, the multimaterial protective shell provides better impact protection from multiple orientations, and protection against granular particles and fluids in the environment. However, the manufacturing process for the multimaterial protective shell requires more complicated molds, as well as multiple thermoforming and assembly steps. If the only desired application of the thermoformed shell is to improve the ability to negotiate obstacles using a streamlined shape, or to provide some impact mitigation in certain orientations, then a simple shell design is suitable.

The stiffness of the structural shell can be tuned to absorb impact energy. With the structural shell, the VelociRoACH can withstand collisions from a four story drop. The flexible layer provides full protection of the robot from granular particles as small as poppy seeds, which could potentially jam the gears or mechanisms. The flexible layer also provides partial protection against water; the electronics and SCM mechanisms of the robot survived 3 min of running through shallow water, although some water was admitted into the resealable version of the bag. The design features, including snap-fit interlocks between the bottom and top structural shell and segmented leg mounts, and the incorporation of a polyethylene zipper bag, make the protective exoskeleton quick to assemble and reusable, which is ideal for both laboratory experimentation and deployment in the field.

We demonstrated manufacturing methods to produce integrated traction enhancing claws in Sec. 6. The claws were cut from fiberglass with a UV ablation laser, in a process taking 35 min for a set of eight, and then bonded onto curved robotic appendages, which took ∼30 s per leg. This process is much more rapid than the shape deposition process used to fabricate claws for previous climbing robots [42].

By incorporating an electronics layer into the robot structure, we enabled the fabrication of tactile sensors made with the SCM process. Two such sensors were developed: one binary hair sensor, and one analog pressure sensor. These integrated sensing structures enable robots to collect tactile information from their immediate surroundings.

In Sec. 8, we demonstrated a scalable process for manufacturing robot legs with integrated, flexible piezoresistive strain gauges. A batch of complete sensors takes 6 hr to build, including all of the disparate cure times. The process is cheap and employable across different substrate materials/geometries, the sensor sensitivity can be tuned based on the ink composition, and the sensor geometry itself is easily customized (the ink is patterned using a laser-cut PET mask). Thus, numerous strain gauges can be integrated into a robot chassis to measure ground reaction forces or body deformations during locomotion.

This paper has shown some of the integrated robotic structures that can be created with the laminar assembly of specialized materials. These material layers were made with accurate and low-cost two-dimensional fabrication processes, and were used to form mechanical linkages, protective exoskeletons, tactile sensors, and force sensing limbs. The simplicity of the fabrication techniques and the minimal requirements for specialty equipment should allow these methods to be widely used. The range of integrated structures that can be made with this manufacturing paradigm is broad and varied.

9.1 Future Work. This work can be extended in two ways: by further improving the developed components, and by making manufacturing methods which are scalable to large production volumes.

The hot-melt reflow process in Sec. 3 greatly reduces the assembly time for SCM structures, but is still dependent on hand assembly. Batch assembly processes which are less wasteful, or

more reliable than current techniques (Refs. [21] and [45], respectively) would further decrease the assembly time. Current SCM robots are dependent on non reel-to-reel compatible components such as the snap-close leg clips in Sec. 5.4. To a certain extent this dependency will exist for any robot, because components such as motors and batteries would be difficult to efficiently produce in such a way. However, there would be fewer required materials and processes if more of a robot's structure could be made with a reel-to-reel compatible process, so it is a worthwhile pursuit for future work.

The protective structures would be improved with a fully waterproof, reclosable flexible shell layer that can resist punctures and tears from impacts and sharp objects. Investigating additional energy absorption components for the structural shell is also a subject of interest. The manufacturing methods used to produce the shells function better for low-volume prototyping methods than mass production. Fabrication techniques which incorporate protective shells with reel-to-reel produced SCM mechanisms would facilitate the rapid manufacture of robust robotic structures.

Some of the manual steps used to fabricate the flexible force sensors can be automated: painting of electrodes can be batch processed using a spray-painting technique to apply the CNT-AgNP ink to the legs. The other fabrication steps are already conducive to batch-manufacture.

Acknowledgment

We would like to thank Shai Revzen for sharing his work on large-scale SCM robots. We would also like to thank Kaushik Jayaram for his insights on shells.

C.C. was responsible for the design, manufacturing, and characterization of the flexible and protective shells in Sec. 5. R.F. directed experiments and edited the paper. D.H. was responsible for Secs. 2–4. He designed the OpenRoACH robot which has been open-sourced with this publication, contributed to the research on claws and the flexible shell, and was the editor of the paper. J.K. developed the force sensing arrays. J.L. was responsible for Sec. 6. C.L. created the shell which enables the traversal of cluttered terrain and identified relevant background research. A.P. assisted with shell manufacturing processes and mechanical design. E.S. was responsible for Sec. 8, with guidance and materials provided by A.J. and H.O. D.Y. specified and performed the material tests, and assembled the composite version of OpenRoACH.

This material is based upon work supported by the National Science Foundation under IGERT Grant No. DGE-0903711, the Graduate Research Fellowship Program, Grant No. CNS-0931463, the NSF NASCENT Center; also by the Miller Institute for Basic Research in Science of UC Berkeley, the DARPA Maximum Mobility and Manipulation program, and the United States Army Research Laboratory under the Micro Autonomous Science and Technology Collaborative Technology Alliance.

References

[1] Spagna, J. C., Goldman, D. I., Lin, P.-C., Koditschek, D. E., and Full, R. J., 2007, "Distributed Mechanical Feedback in Arthropods and Robots Simplifies Control of Rapid Running on Challenging Terrain," Bioinspiration Biomimetics, **2**(1), pp. 9–18.

[2] Li, C., Pullin, A. O., Haldane, D. W., Fearing, R. S., and Full, R. J., 2015, "Shape-Assisted Body Reorientation in Animals and Robots Enhances Traffickability Through Cluttered Terrain," Bioinspiration Biomimetics (in press).

[3] Jayaram, K., Mongeau, J. M., McRae, B., and Full, R. J., 2010, "High-Speed Horizontal to Vertical Transitions in Running Cockroaches Reveals a Principle of Robustness," Annual Meeting, Society for Integrative and Comparative Biology, Seattle, WA, Jan. 3–7.

[4] Shimada, E., Thompson, J. A., Yan, J., Wood, R. J., and Fearing, R. S., 2000, "Prototyping Millirobots Using Dextrous Microassembly and Folding," ASME IMECE/DSCD, Orlando, FL, Nov. 5–10.

[5] Wood, R. J., Avadhanula, S., Menon, M., and Fearing, R., 2003, "Microrobotics Using Composite Materials: The Micromechanical Flying Insect Thorax," IEEE International Conference on Robotics and Automation (ICRA '03), Taipei, Taiwan, Sept. 14–19, pp. 1842–1849.

[6] Hoover, A. M., and Fearing, R. S., 2008, "Fast Scale Prototyping for Folded Millirobots," IEEE International Conference on Robotics and Automation (ICRA 2008), Pasadena, CA, May 19–23, pp. 886–892.

[7] Wood, R. J., Avadhanula, S., Sahai, R., Steltz, E., and Fearing, R. S., 2008, "Microrobot Design Using Fiber Reinforced Composites," ASME J. Mech. Des., **130**(5), p. 052304.

[8] Pullin, A., Kohut, N. J., Zarrouk, D., and Fearing, R. S., 2012, "Dynamic Turning of 13 cm Robot Comparing Tail and Differential Drive," IEEE International Conference on Robotics and Automation (ICRA), St. Paul, MN, May 14–18, pp. 5086–5093.

[9] Birkmeyer, P. M., Peterson, K., and Fearing, R. S., 2009, "DASH: A Dynamic 16g Hexapedal Robot," IEEE International Conference on Intelligent Robots and Systems (IROS 2009), St. Louis, MO, Oct. 10–15, pp. 2683–2689.

[10] Hoover, A. M., Burden, S., Fu, X. Y., Sastry, S. S., and Fearing, R. S., 2010, "Bio-Inspired Design and Dynamic Maneuverability of a Minimally Actuated Six-Legged Robot," 3rd IEEE/RAS and EMBS International Conference on Biomedical Robotics and Biomechatronics (BioRob), Tokyo, Sept. 26–29, pp. 869–876.

[11] Haldane, D. W., Peterson, K. C., Garcia Bermudez, F. L., and Fearing, R. S., 2013, "Animal-Inspired Design and Aerodynamic Stabilization of a Hexapedal Millirobot," IEEE International Conference on Robotics and Automation (ICRA), Karlsruhe, Germany, May 6–10, pp. 3279–3286.

[12] Haldane, D. W., and Fearing, R. S., 2014, "Roll Oscillation Modulated Turning in Dynamic Millirobots," IEEE International Conference on Robotics and Automation (ICRA), Hong Kong, May 31–June 7, pp. 4569–1575.

[13] Kohut, N. J., Peterson, K. C., Zarrouk, D., and Fearing, R. S., 2013, "Aerodynamic Steering of a 10 cm High-Speed Running Robot," IEEE/RSJ International Conference on Intelligent Robots and Systems (IROS), Tokyo, Nov. 3–7, pp. 5593–5599.

[14] Birkmeyer, P. M., Gillies, A. G., and Fearing, R. S., 2011, "CLASH: Climbing Vertical Loose Cloth," 2011 IEEE/RSJ International Conference on Intelligent Robots and Systems (IROS), San Francisco, CA, Sept. 25–30, pp. 5087–5093.

[15] Birkmeyer, P., Gilles, A. G., and Fearing, R. S., 2012, "Dynamic Climbing of Near-Vertical Smooth Surfaces," IEEE/RSJ International Conference on Intelligent Robots and Systems (IROS), Vilamoura, Portugal, Oct. 7–12, pp. 286–292.

[16] Boothroyd, G., Dewhurst, P., and Knight, A., 2002, *Product Design for Manufacture and Assembly*, CRC Press, Boca Raton, FL.

[17] Hoover, A., and Fearing, R., 2009, "Analysis of Off-Axis Performance of Compliant Mechanisms With Applications to Mobile Millirobot Design," IEEE/RSJ International Conference on Intelligent Robots and Systems (IROS 2009), St. Louis, MO, Oct. 10–15, pp. 2770–2776.

[18] Ma, K. Y., Felton, S. M., and Wood, R. J., 2012, "Design, Fabrication, and Modeling of the Split Actuator Microrobotic Bee," IEEE/RSJ International Conference on Intelligent Robots and Systems (IROS), Vilamoura, Portugal, Oct. 7–12, pp. 1133–1140.

[19] Guérinot, A. E., Magleby, S. P., Howell, L. L., and Todd, R. H., 2005, "Compliant Joint Design Principles for High Compressive Load Situations," ASME J. Mech. Des., **127**(4), pp. 774–781.

[20] Whitney, J. P., Sreetharan, P. S., Ma, K. Y., and Wood, R. J., 2011, "Pop-Up Book MEMS," J. Micromech. Microeng., **21**(11), p. 115021.

[21] Sreetharan, P. S., Whitney, J. P., Strauss, M. D., and Wood, R. J., 2012, "Monolithic Fabrication of Millimeter-Scale Machines," J. Micromech. Microeng., **22**(5), p. 055027.

[22] Baisch, A. T., Ozcan, O., Goldberg, B., Ithier, D., and Wood, R. J., 2014, "High Speed Locomotion for a Quadrupedal Microrobot," Int. J. Rob. Res. (in press).

[23] Sahai, R., Lee, J., and Fearing, R., 2003, "Semi-Automated Micro Assembly for Rapid Prototyping of a One DOF Surgical Wrist," IEEE/RSJ International Conference on Intelligent Robots and Systems (IROS 2003), Las Vegas, NV, Oct. 27–31, pp. 1882–1888.

[24] Karrer, P., and Hofmann, A., 1929, "Polysaccharide XXXIX. Über den enzymatischen Abbau von Chitin und Chitosan I," Helv. Chim. Acta, **797**(1925), pp. 84–86.

[25] Hoffman, K. L., and Wood, R. J., 2011, "Passive Undulatory Gaits Enhance Walking in a Myriapod Millirobot," IEEE/RSJ International Conference on Intelligent Robots and Systems (IROS), San Francisco, CA, Sept. 25–30, pp. 1479–1486.

[26] Mehta, A., and Rus, D., 2014, "An End-to-End System for Designing Mechanical Structures for Print-and-Fold Robots," IEEE/RSJ International Conference on Robotics and Automation (ICRA), Hong Kong, May 31–June 7, pp. 1460–1465.

[27] Soltero, D., Julian, B., Onal, C. D., and Rus, D., 2013, "A Lightweight Modular 12-DOF Print-and-Fold Hexapod," IEEE/RSJ International Conference on Intelligent Robots and Systems (IROS), Tokyo, Nov. 3–7, pp. 1465–1471.

[28] Hoover, A., Steltz, E., and Fearing, R., 2008, "RoACH: An Autonomous 2.4 g Crawling Hexapod Robot," IEEE/RSJ International Conference on Intelligent Robots and Systems (IROS 2008), Nice, France, Sept. 22–26, pp. 26–33.

[29] Noh, M., Kim, S.-W., An, S., Koh, J.-S., and Cho, K.-J., 2012, "Flea-Inspired Catapult Mechanism for Miniature Jumping Robots," IEEE Trans. Rob., **28**(5), pp. 1007–1018.

[30] Hirata, K., 2000, "Development of Experimental Fish Robot," Sixth International Symposium on Marine Engineering (ISME 2000), Tokyo, Japan, Oct. 23–27, pp. 235–240.

[31] Guo, S., Fukuda, T., and Asaka, K., 2003, "A New Type of Fish-Like Underwater Microrobot," IEEE/ASME Trans. Mechatron., **8**(1), pp. 136–141.

[32] Fish, F. E., Lauder, G. V., Mittal, R., Techet, A. H., Triantafyllou, M. S., Walker, J. A., and Webb, P. W., 2003, "Conceptual Design for the Construction

of a Biorobotic AUV Based on Biological Hydrodynamics," 13th International Symposium on Unmanned Untethered Submersible Technology, Durham, NH, Aug. 24–27.
[33] Lachat, D., Crespi, A., and Ijspeert, A. J., 2006, "Boxybot: A Swimming and Crawling Fish Robot Controlled by a Central Pattern Generator," 1st IEEE/RAS-EMBS International Conference on Biomedical Robotics and Biomechatronics (BioRob 2006), Pisa, Italy, Feb. 20–22, pp. 643–648.
[34] Kovač, M., Schlegel, M., Zufferey, J.-C., and Floreano, D., 2010, "Steerable Miniature Jumping Robot," Auton. Rob., **28**(3), pp. 295–306.
[35] Floreano, D., Zufferey, J.-C., Klaptocz, A., Germann, J. M., and Kovac, M., 2011, "Aerial Locomotion in Cluttered Environments," 15th International Symposium on Robotics Research, Flagstaff, AZ, Aug. 28–Sept. 1.
[36] Klaptocz, A., Briod, A., Daler, L., Zufferey, J.-C., and Floreano, D., 2013, "Euler Spring Collision Protection for Flying Robots," IEEE/RSJ International Conference on Intelligent Robots and Systems (IROS), Tokyo, Japan, Nov. 3–7, pp. 1886–1892.
[37] Karwoski, K., 2011, "Quadrocopter Control Design and Flight Operation," NASA Marshall Space Flight Center, Huntsville, AL, Technical Report No. M11-0980.
[38] Wang, C., Nahon, M., and Trentini, M., 2014, "Controller Development and Validation for a Small Quadrotor With Compensation for Model Variation," International Conference on Unmanned Aircraft Systems (ICUAS), Orlando, FL, May 27–30, pp. 902–909.
[39] O'Halloran, D., Wolf, A., and Choset, H., 2005, "Design of a High-Impact Survivable Robot," Mech. Mach. Theory, **40**(12), pp. 1345–1366.
[40] Li, C., and Full, R. J., 2014, "Insects Traversing Grass-Like Vertical Compliant Beams," Society for Integrative and Comparative Biology Annual Meeting, Austin, TX, Jan. 3–7.
[41] Autum, K., Buehler, M., Cutkosky, M. R., Fearing, R. S., Full, R. J., Goldman, D. I., Groff, R., Provancher, W., Rizzi, A. A., Saranli, U., Saunders, A., and Koditschek, D. E., 2005, "Robotics in Scansorial Environments," Proc. SPIE, **5804**, pp. 291–302.
[42] Asbeck, A. T., Kim, S., Cutkosky, M. R., Provancher, W. R., and Lanzetta, M., 2006, "Scaling Hard Vertical Surfaces With Compliant Microspine Arrays," Int. J. Rob. Res., **25**(12), pp. 1165–1179.
[43] Karras, J. T., Haldane, D. W., and Fearing, R. S., 2012, "Rapid-Manufacturable Hair Sensor Array for Legged Millirobots," IEEE/RSJ International Conference on Intelligent Robots and Systems (IROS), Vilamoura, Portugal, Oct. 7–12, pp. 1956–1962.
[44] Takei, K., Yu, Z., Zheng, M., Ota, H., Takahashi, T., and Javey, A., 2014, "Highly Sensitive Electronic Whiskers Based on Patterned Carbon Nanotube and Silver Nanoparticle Composite Films," Proc. Natl. Acad. Sci. U.S.A., **111**(5), pp. 1703–1707.
[45] Felton, S., Tolley, M., Demaine, E., Rus, D., and Wood, R., 2014, "A Method for Building Self-Folding Machines," Science, **345**(6197), pp. 644–646.